MONASH University

Synthesis and doping modification of Ultrathin WSe2/WS2 Heterostructure

Zhipeng Li
Master by Research

A thesis submitted for the degree of Master at
Monash University in 2016
Material Engineering in Monash University

Copyright notice

I certify that I have made all reasonable efforts to secure copyright permissions for third-party content included in this thesis and have not knowingly added copyright content to my work without the owner's permission.

Signed ____________________________

Date ______________________________

MONASH University

Declaration

This thesis contains no material which has been accepted for the award of any other degree or diploma at any university or equivalent institution and that, to the best of my knowledge and belief, this thesis contains no material previously published or written by another person, except where due reference is made in the text of the thesis.

Signed ____ [redacted] __

Print Name: Zhipeng Li

Date Aug. 10th 2016

Abstract

Two-dimensional material such as graphene is reported to be outstanding example with remarkable properties, including surprisingly high carrier mobility, extraordinary thermal conductivity and great optical transmittance. However, the limitation of graphene urge us focus on ultrathin layered semiconductors made by transition metal dichalcogenides (TMDCs) such as WS_2 and WSe_2. It possesses outstanding optical and optoelectronics properties. Apart from making pure single crystal, manufacturing of lateral heterostructure with two different TMDC semiconductors is another promising way to exploring the full potential of these layered materials. This thesis report concludes the development history of two dimensional materials from the discovery of graphene, the basic knowledge gap of TMDC to the research of TMDC heterostructure.

After that, in this report, a noval single-step chemical vapor deposition (CVD) method for epitaxial growth and selective substitution of lateral WSe_2/WS_2 heterostructures with its growth mechanism are presented. For characterization of resulting heterostructure, Raman, photoluminescence mapping and atomic force microscopy (AFM) were obtained to prove that it is atomically thin lateral heterostructure. Furthermore, detailed Photoluminence (PL) characterisation and Scanning photoelectron microscopy (SPEM) mapping are utilized to study on bonding energy which is direct related to the band shifting and doping module. Electrical characterisation on fabricated device is then report to illustrate the performance of this heterostructure flake. Those studies aims at providing basis of understanding of new single-step synthesis method and the variety of properties of formed heterostructure.

Acknowledgements

Firstly, I would like to express my deepest gratitude to my supervisor Dr Qiaoliang Bao for his full support to my master research in the last two years. His patience, enlightening suggestions and profound knowledge helps me a lot when I was facing the difficulties in the road of scientific research. His altruistic assistance provided me the last hope when I gave my determination during the last two years of study.

Besides, I am indebted to Dr Jiao Lin and Prof Michael Fuhrer after they gave me the rare opportunity in master study in Monash Univeristy.

Also, I would like to thank the staff in MCN, Dr John Zhu, Dr Yang Lim Hemayet Uddin for training me the research facility. Without their help, I would not be possible to conduct those researches.

I would thank Dr Wei-Yen Woon, Dr Chuang Min-Chiang from National Central University and Chia-Hao Chen in National Synchrotron Riadiation Centre in ROC for their outstanding result of XPS research.

I would like to give my appreciation to my college, Dr Yupeng Zhang, Mr Zaiquan Xu, Mr Jingchao song, Mr Jialu Zheng and any other fellows that contribute to this research as well as article writing.

Last but not the least, I would like to thank my family, friends and all those whose kindness and advice have made this work possible.

List of Figure

density

Figure 3e: Calculated and measured carrier mobility in multilayer MoS_2 as a function of temperature

Figure 4a: Thickness-dependent Raman spectra for MoS_2

Figure 4b: Peak position shifts for the E^1_{2g} and A_{1g} modes as a function of MoS_2 layer thickness for the spectra in figure 4a

Figure 4c-d: Absorption and photoluminescence spectra of MoS_2 thin films

Figure 5a: Schematic atomic side view of typical two-dimensional multilayered heterostructure.

Figure 5b: The band alignment at the K-point for the WS_2/MoS_2 heterostructure.

Figure 5c: Schematic images of the vertically stacked WS_2/MoS_2 heterostructures synthesized at 850℃

Figure 5d: Schematic images of the lateral connected WS_2/MoS_2 heterostructures synthesized at 650℃

Figure 5e: Typical plot of gating voltage versus source/drain current of a CVD-grown WS_2/MoS_2 bi-layer, a mechanically transferred WS_2/MoS_2 bilayer, a MoS_2 bilayer and monolayer MoS_2 samples

Figure 6a: Schematic of MoS2/Graphene based Li ions battery

Figure 6b: Schematic drawing of the MoS_2/WSe_2 vertical heterostructure device

Figure 6c: J−V characteristics of the device under optical illumination,

Figure 6d: I_{ds}–V_{ds} output characteristics of a WS_2 FET at various backgate voltages.

Figure 6e: I_{ds}–V_{ds} output characteristics of a WSe_2 FET at various backgate voltages

Figure 6f: Gate-tunable output characteristics of a lateral WSe_2/WS_2 heterostructure p–n diode. Scale bar, 2 μm

Figure 6g: Experimental output (I_{ds}–V_{ds}) characteristics of the lateral WSe_2/WS_2 heterostructure p–n diode

Figure 6h: Scanning photocurrent mapping image of the lateral WSe_2–WS_2 heterostructure p–n diode

Figure 6i: A CMOS inverter obtained by integrating a p-type WSe_2 and n-type WS_2 FET

Figure 7a: Optical image taken from a vertical WS_2/MoS_2 heterostructure prepared by PDMS stamping of CVD grown WS_2 onto MoS_2 monolayer.

Figure 7b-c: Raman mapping at the A'_1 mode, 408 cm^{-1} (MoS_2) and 421 cm^{-1} (WS_2)

Figure 7d-e: PL mapping at 1.85 (MoS_2) and 2.01 eV (WS_2).

Figure 7f-g: Raman and PL spectra of MoS_2 and WS_2 monolayers and an as-transferred WS2 /MoS2 heterostructure

Figure 8a: AFM image of a triangular domain with a thickness of 1.2 nm. Inset: optical image of a triangular domain

Figure 8b: Raman spectra of a heterostructure domain

Figure 8c: Photoluminescence spectra of a heterostructure domain

Figure 8d: Raman mapping at 419 cm^{-1} (WS_2 A_{1g} signal)

Figure 8e: Raman mapping at 256 cm^{-1} (WSe_2 A_{1g} signal)

Figure 8f: Composite image consisting of Raman mapping at 256 cm^{-1} and 419 cm^{-1}

Figure 8g-h: Photoluminescence mapping images at 665 nm and 775 nm, characteristic photoluminescence emission of WS_2 and WSe_2 respectively

Figure 8g-h: Composite image consisting of photoluminescence mapping at 665 nm and 775 nm

Figure 9a: Raman spectra of WS_2, MoS_2, and their vertical heterojunction

Figure 9b: Optical microscope images of the MoS_2/WS_2 vertical heterostructure device

Figure 9c-d: Raman maps of integrated intensities of peaks at 351 and 382 cm^{-1}. Data were collected from the black box in panel b, with a scanning area of 80×80 μm^2

Figure 9e: Single PL spectra of MoS_2, WS_2, and their vertical structure.

Figure 9f: PL mapping of MoS_2/WS_2 vertical heterostructure, collected from the white box in panel b, with a scanning area of 21×21 $\mu m^{2.}$

Figure 10: Schematic of CVD system and heating profile

Figure 11: Schematic of the PL facility

Figure 12a: Schematic diagram of CVD system set up for the chemical synthesis of doped WSe_2/WS_2 heterostructure

Figure 12b: Temperature profile of heating belt (first heating region) and furnace (second heating region) among growth and substitution procedure to form doped WSe_2/WS_2 heterostructure.

Figure 12c: Optical Image of WSe_2/WS_2 heterostructure flake.

Figure 12d: Size and thickness distribution of resulting heterostructure flake.

Figure 12e: Raman spectrum which is taken from the centre and periphery region of WSe_2/WS_2 heterostructure

Figure 12f: PL spectrum of doped heterostructure on the centre and edge

Figure 12g-h: Raman mappings that are taken among the entire flake base on WS_2 and

WSe_2 E^1_{2g} vibration mode.

Figure 12i: AFM gained height diagram among the half of heterostructure.

Figure 12j: The phase image obtained from AFM tip mode

Figure 13a-c: The optical image of resulting heterostructure, Raman mapping of $WS_2E^1_{2g}$ vibration mode and Raman mapping of $WSe_2E^1_{2g}$ vibration mode of heterostructure that is made with holding time is about 30 minutes.

Figure 13d-f: The optical image of resulting heterostructure, Raman mapping of $WS_2E^1_{2g}$ vibration mode and Raman mapping of $WSe_2E^1_{2g}$ vibration mode of heterostructure that is made with holding time is about 90 minutes

Figure 13g-i: The optical image of resulting heterostructure, Raman mapping of $WS_2E^1_{2g}$ vibration mode and Raman mapping of $WSe_2E^1_{2g}$ vibration mode of heterostructure that is made with holding time is about 120 minutes.

Figure 14a-b: PL mapping of WSe2/WS2 heterostructure based on 620nm to 680nm and based on 680nm to 740nm. Inset shows the direction of line scanning of PL spectra from a to g, the point d is located in the interface between WSe_2 and WS_2.

Figure 14c: PL spectra that is taken from point a to g mark with different color.

Figure 14d: AFM result among the one edge of triangular domain indicates the sapphire, WS_2 and WSe_2

Figure 14e: Surface potential mapping corresponding to AFM shown in figure 6d.

Figure 14f: Surface potential profile along x-axis of figure 6e

Figure 15a-c: XPS spectra to characteristic peak of W, Se and S

Figure 15d-f: XPS mapping on W4f, Se3d and S2p element orbit with SPEM.

Figure 15g-j: binding energy and binding energy shift taken from the centre of heterostructure marked with XPS 7, 8, 9.

Figure 15k-n: bind energy and binding energy shift taken from the rim of heterostructure marked with XPS 2, 3, 4, 5

Figure 16a-c: Schematic diagram to show the mechanism of different growth procedure 1, 2 and 3

Figure 16d-e: Raman mapping on E^1_{2g} vibration mode of WS_2 and WSe_2 on a sample made in procedure 2

Figure 16f: Raman spectra taken from centre and periphery on a sample made in procedure 2.

Figure 16g-h: Raman mapping on E^1_{2g} vibration mode of WS_2 and WSe_2 on a sample made in procedure 3

Figure 16i: Raman spectra taken from centre and periphery on a sample made in procedure 3.

Figure 17a: Schematic diagram of fabricated device

Figure 17b: Gate induced test

Figure 17c: Electrical transport curves (I versus V) with different light exposure

Figure 17d: Electrical photoresponse test among WSe2/WS2 heterostructure

Figure 17e: Dependence of photocurrent and photoresponsivity on incident light power

Table of Content

Chapter 1: Introduction

1.1 Two-dimensional nanomaterial

1.1.1 Introduction to two-dimensional nanomaterial

With the development of technology in fundamental physics, chemistry, microstructure observation, precise parameter control synthesis, and multiple feasible characterisation method, the traditional bulk material such as metal construction materials, ceramic bulk and block polymer compound have been encountering thoroughly research after long period of study. In this occasion, scientists and researchers are urged to propose material with newly discovered nanotechnology for exploring the novel potential material. Nano-related researches are then presented to realize the material units with at least one dimension of nano-scale in three-dimensional spacing which is then called nanomaterial.

This specific type of material, with typical mesoscopic system, possessing special surface effect, small-size effect and macroscopic quantum tunneling effect, sees the dramatic increment of surface area and surface activity of nanomaterial, when it is separated from bulk material. In that case, exotic properties are supposed to be displayed on a nanomaterial, when macroscopic objects are subdivided into ultrafine particles with nano-scale. In other words, the optical, thermal, electrical, magnetic, mechanical and chemical behavior of nano-scaled particles will be significantly different from its corresponding bulk material.

Generally, the nanomaterial can be divided into numerous categories based on the dimensional topological spacing difference such as zero-dimensional nanomaterial, one-dimensional nanomaterial, two-dimensional nanomaterial and three-dimensional nanomaterial.

Two-dimensional topological materials, or two-dimensional materials, are crystalline materials consisting of layered arranged atoms or molecules. this particular type of materials such as nanofilms, super-lattices and quantum wells, only allow for the non-nanoscaled electrons movement in plane direction which results in the anisotropy between the plane direction and vertical direction. They are promising candidate for application such as electrode, semiconductors and photovoltaics due to their unique performance

1.1.2. Graphene

In 2004, the successful production of atomically thin carbon layer by mechanical exfoliation has been hailed as the milestone for research of two-dimensional material and expanded the frontier of two-dimensional material research[1]. This carbon layer, so-called graphene, is an allotrope of carbon that illustrates a structure of a two-dimensional, atomic-scale, hexagonal and non-metallic crystal which has thickness less than 1 nm which is shown in **Figure 1**a.

The intrinsic characteristics of graphene such as double cone band structure and quantum tunneling effect of monolayer carbon electron provides abundant of new physics and less constraint on electron movement and molecular vibration. According to the previous research, the unique structure of Graphene illustrate outstanding performance such as extremely high

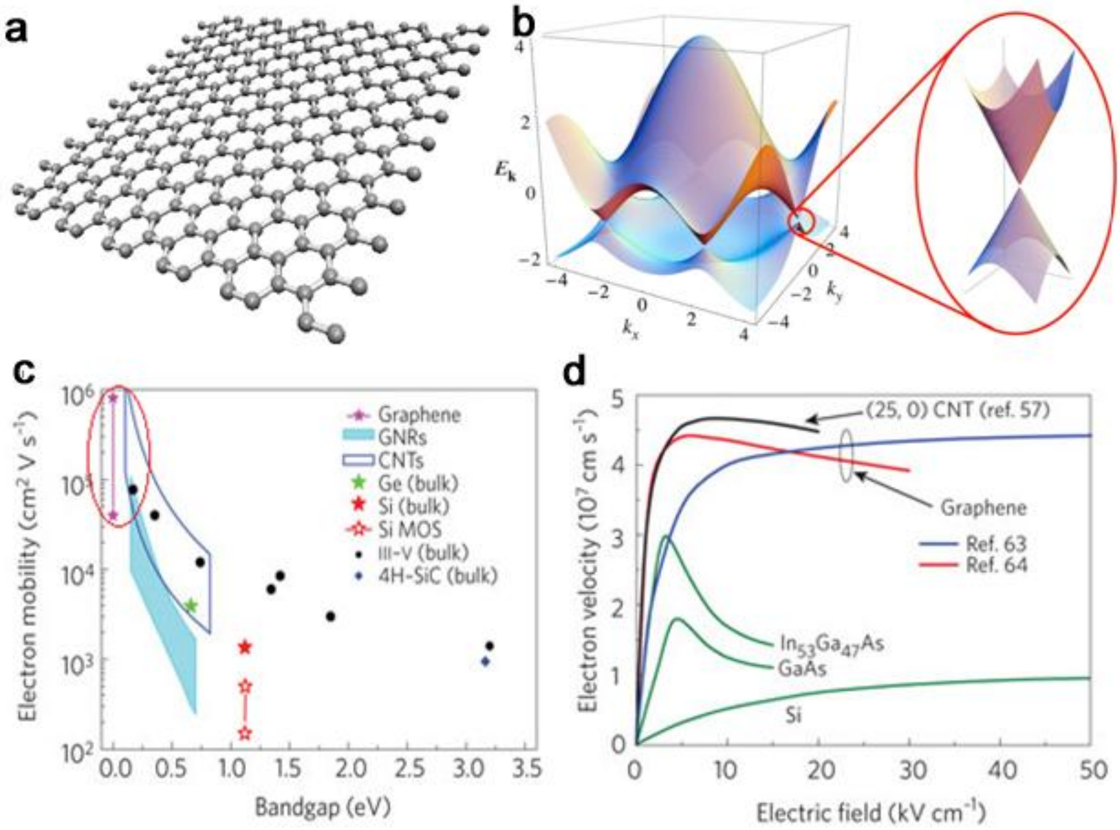

Figure 1. (a) Ball-and-stick schematic image of carbon atom arrangement in graphene. (b) Double Dirac cone around K point in two-dimensional band structure of graphene. (c) Electron mobility versus bandgap in low electric fields for different materials, as indicated (from left to right, iii–v compounds are InSb, InAs, $In_{0.53}Ga_{0.47}As$, InP, GaAs, $In_{0.49}Ga_{0.51}P$, and GaN). (d) Electron drift velocity versus electric field for common semiconductors (Si, GaAs, In0$_{.53}$Ga0.$_{47}$As), a carbon nanotube and large-area graphene. [2-4]

----

carrier mobility (15000 cm^2/V S) (as shown in **figure 1**c-d), high thermal conductivity (5300 W/m K) and high transmittance (97.7%) [2-4]. Those outstanding performance allures substantial attention on Graphene based research in optical and electronic application such as solar cell, optical modulator, photodetector and mode-lock laser, however, the absence of bandgap in Graphene band structure impede the application of intrinsic graphene. The zero bandgap provides little ability for cutting off the current while negative bias is applied and it is incapable for exciton disassociation like semiconductors[5]. Therefore, chemical or physical modifications for band engineering are usually applied to introduce novel performance and further improvement [2-4, 6-9].

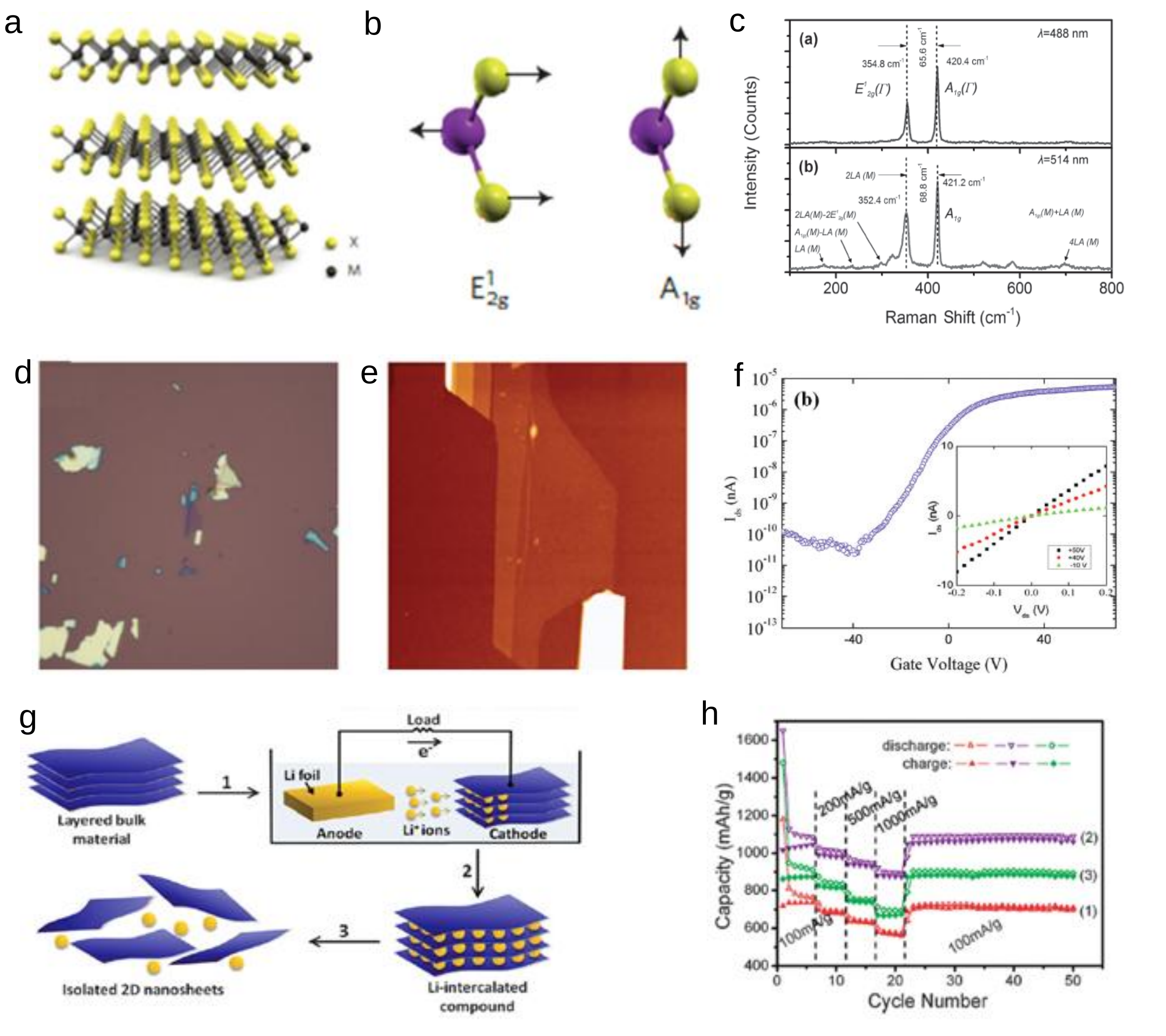

Figure 2. (a) Three-dimensional schematic representation of a typical MX2 structure, with the chalcogen atoms (X) in yellow and the metal atoms (M) in grey[10]. (b) Vibration mode of TMDC material E^1_{2g} and A_{1g}[11]. (c) Characteristic peak of WS_2 in Raman spectrum acquired with laser excitation of λ = 488 nm for the WS_2 film grown on quartz [12]. (d-e) Optical image and tapping mode AFM image of a mechanical exfoliated WS_2 flake [13]. (f) Logarithmic conductance as a function of gate voltage with I_{on}/I_{off} = 100 000 at V_b = 0.1 V. Inset: drain current I_{ds} versus drain voltage V_{ds} for various gate voltages [13]. (g) Electrochemical lithiation and exfoliation process for fabrication of 2D nanomaterials from the layered bulk crystals [14]. (h) Rate capability of MoS2/rGO samples at different current density: (1) MoS_2/rGO (1: 1); (2) MoS_2/rGO (1: 2); (3) MoS_2/rGO (1: 4). [2-4, 6-9]

1.1.3 TMDCs

Although nanostructuring and chemical modification can introduce bandgap in graphene, the sacrifice of other properties such as conductivity and stability has to be made. Therefore, this urges scientists to find out other two-dimensional material, for example, graphene analogue boron nitride (BN) [15-17], transition metal oxide (TMO), such as titanium oxide or perovskite [17-19], and transition metal dichalcogenides (TMDC). Among those materials, TMDCs are recognized as one of the most promising materials in electronic and photonic application.

1.1.3.1 Structure of TMDC heterostructure

TMDCs semiconductor, known as a type of two-dimensional material, have attracted substantial attention and been considered as the most potential material in next generation of optoelectronic devices, because of their outstanding, layer-number dependent optoelectronics properties [11, 20]. They are often represents as MX_2, where M is transition metal which is usually group-V element (V, Ta, Nb) or group-VI element (Mo, W and so on), and X is chalcogen (S, Se, Te and etc.).

Among all the TMDC materials, WS_2 is one of the prime examples. It has layered structure which is the counterpart of graphite. Each layer has similar X-M-X staked structure with interlamellar spacing of about 7-8 Å, which is shown in **Figure 2**a [21]. This structure determines two major vibration modes in a typical single layer TMDC material as shown in **figure 2**b, the main Raman peaks correspond to the E^1_{2g} in-plane vibration modes, and the A_{1g} inter-plane vibration mode (**Figure 2**c). The characteristic peak of Raman varies in different types of TMDC, hence the identification of TMDC material can be applied with Raman spectroscopy. They are found to be the counterpart of graphene, with reasonable high mobility and variety of band structure. They also provide novel and outstanding phenomena such as high on/off ratio, indirect to direct bandgap transition, large exciton binding energy and strong photoluminescence which are notably different from those of their bulk materials.

In recent years, high-qualified TMDCs single crystals were processed to fabricate electronic optoelectronic devices, as much like traditional silicon semiconductor. [12, 21-30] Great achievements have been made recently, including making transistor, light emitting diode (LED) and photodetector. However, the quantum efficiency of photoelectric or electroluminescence transition are conventionally low, which should therefore requires effective separation or injection of electrons and holes within a *p-n* junction.

1.1.3.2 Properties and applications of TMDC material

Although, bulk TMDC materials were introduced to the public in decade years ago and were widely used in electronics, photonics, chemical and catalytic areas, two-dimensional TMDCs research was just at their beginning in recent year. Simulation calculation in 2011 about TMDC material indicates that, with help of quantum confinement on electronics structure, the indirect band gap in bulk TMDC material turns to direct band gap in 2D TMDC material (**Figure 3**a) [11, 31]. This leads to extraordinary change in photonics and electronic properties which brings in promising technological potential, especially for electronics, photonics and catalysis application.

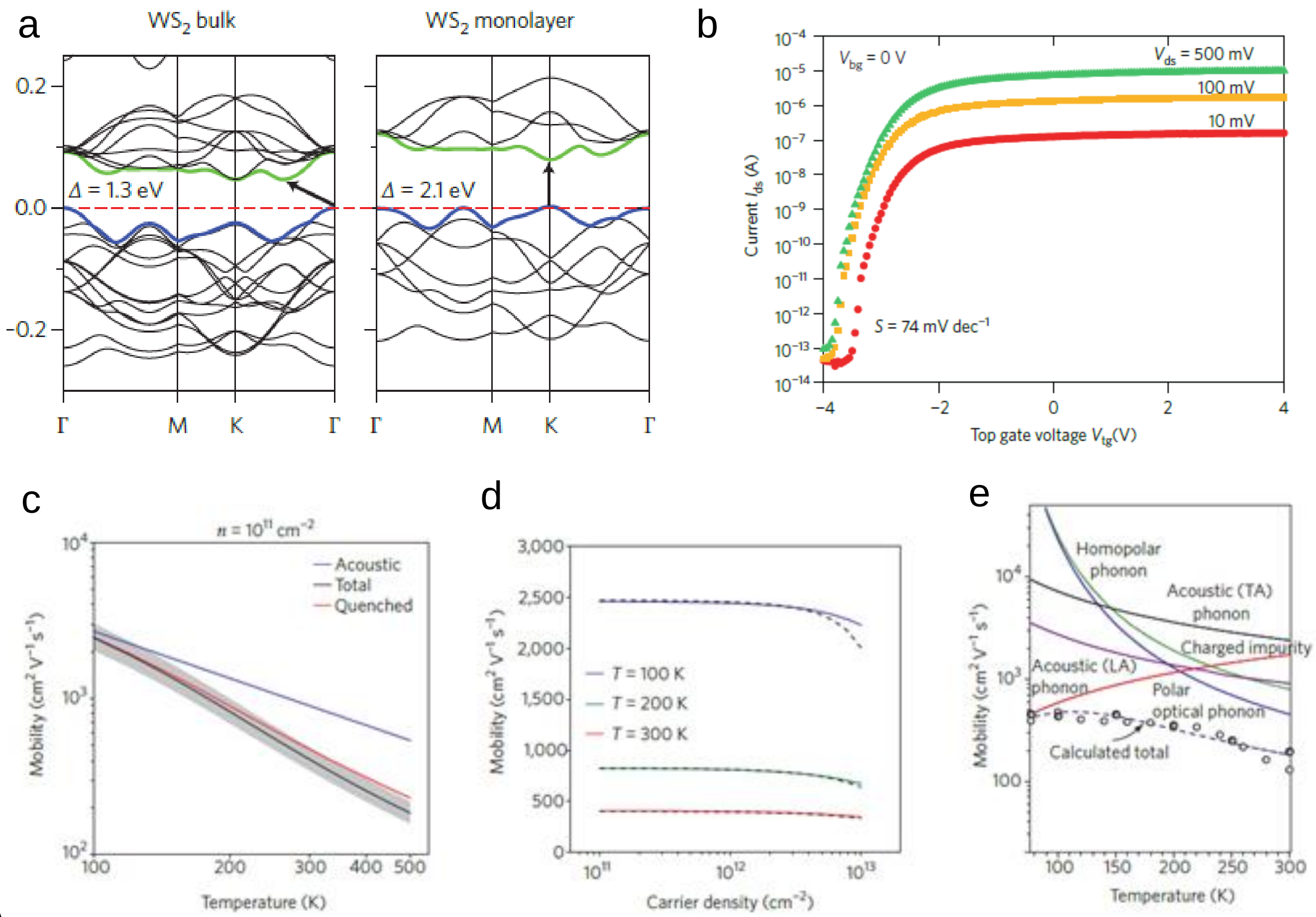

\

Figure 3. (a) Band structures calculated from first-principles density functional theory (DFT) for bulk and monolayer WS_2 [31]. (b) Source–drain current (I_{ds}) versus top gate voltage (V_{tg}) curve recorded from the top-gated device for a bias voltage ranging from 10 mV to 500 mV. [21]. (c-d) Carrier mobility in monolayer MoS_2 as a function of temperature and carrier density [32]. (e) Calculated and measured carrier mobility in multilayer MoS_2 as a function of temperature [33].

The electrical properties [18, 21, 31-35] of intrinsic single layer TMDC material is the semiconductor with direct band gap, having a band width of about 1.1-1.9 eV that is similar to silicon (1.1ev) as shown in **Figure 3**a. This makes that TMDC material an alternative to replace traditional Si material in electronic component. Current–voltage curves for this FET are shown in **Fig. 3**b to illustrate that the top-gated geometry allows for a reduction in the voltage necessary to switch the device while allowing the integration of multiple devices on the same substrate. The carrier mobility dependent on temperature in single-layer MoS2 calculated from first principles is shown in **Figure 3**c [32]. The electron

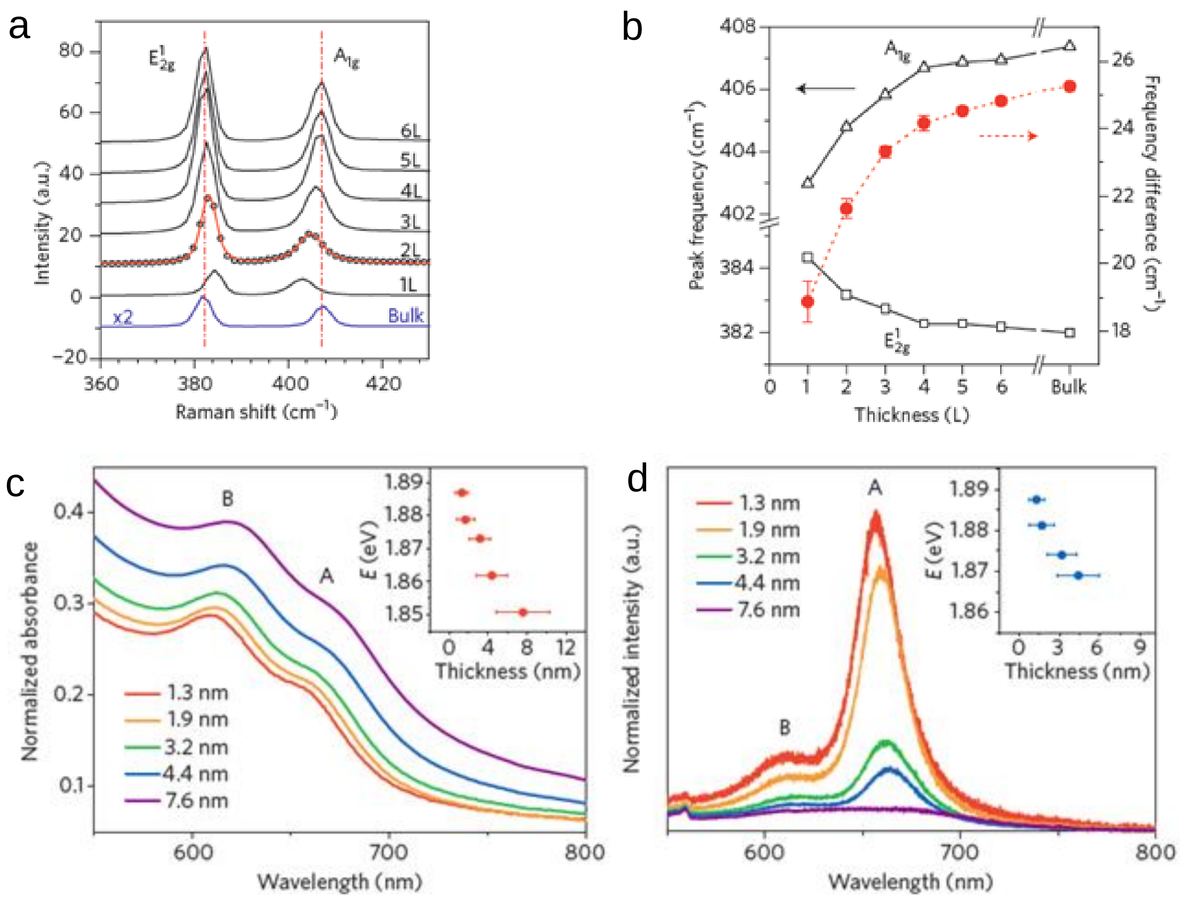

Figure 4. (a) Thickness-dependent Raman spectra for MoS_2 [36]. (b) Peak position shifts for the E12g and A1g modes as a function of MoS2 layer thickness for the spectra in figure 4a [36]. (c-d) Absorption and photoluminescence spectra of MoS2 thin films with average thicknesses ranging from 1.3 to 7.6 nm. Insets: energy of the A exciton peak as a function of average film thickness [37].

---

mobility is dominated by acoustic component but when temperature is ramping, the optical component play more important role. carrier concentration theoretical calculation confirmed that the on/off ratio MoS_2 film with HfO_2 dielectric layer can reach more than 1×10^8 with low energy consumption [38]. It also avoids short channel effect which gives the possibility to make smaller device. MoS_2 single crystal transistors can also be used to make logic circuit to realize static storage. Apart from that, 2D TMDC material has lower resistance to embedding lithium which provide channel for transporting of lithium ions. Those properties allows for high electric capacity and long lifetime lithium ion battery [39]. The effect of carrier concentration and temperature on electron mobility of MoS_2 is shown in **Fig. 3d**. The combined effect of phonons and charged impurities on the mobility of multilayer MoS_2 is shown in **Fig. 3e**, and shows a similar general trend to that of monolayer MoS_2

The optical properties (Figure 4a-d) [11, 29, 31, 36, 37, 40] are dramatically changed with the indirect band gap in bulk TMDC material turning into direct bandgap in single layer TMDC material, with the PL peak of the monolayer MoS_2 at 1.9 eV, as seen in **Fig. 4d**. This owes to the thoroughly taking advantage of light with direct band gap, which resulting in the increment of efficiency of light absorption and divergence of semiconductor. Those changes are mainly represents in Raman, Photoluminescence (PL) and electroluminescent (EL) spectrum. When layer number is decreasing, the A_{1g} vibration mode near 406 cm^{-1} is left-shifted while the E^1_{2g} peak shifts to the right direction (**Fig. 4**a) [36]. The production efficiency of quantum phonon from PL in 2D TMDC material is more than 10000 times more than that in bulk material. In the mean time, 2D TMDC materials also have good light sensitivity. Experiment shows that a phototransistor made by single layer MoS2 crystal has photosensitivity of about 7.5mA/W which is about 7 times more than that of graphene device. Apart from that, TMDC material can also be potential in LED device fabrication which was reported recently. The photo-detector, exchanger and photo-sensor based on TMDC materials may reveal extraordinary performance.

The sensing performance [11, 41, 42] of TMDC is known for its advantage in several aspects. Firstly, the specific area of 2D structure can enhance the concentration detection limits. Secondly, high switch respond of and high carrier mobility of 2D TMDC semiconductors improve the speed of respond of fabricated devices. Then, high strength and toughness of this type of materials allows for making flexible sensing device. Finally, the enhancement of detection sensitivity can be feasible by chemical modification because of its high chemical surface activity. All those outstanding properties are importance for fabricating ultra-high sensitivity and speed of respond sensor. A mechanical exfoliated MoS2 based FET was proved to have minimal detecting limits of about 0.013mg/m^3.

To be summarized, graphene analogue TMDC materials show their distinction in electrics, mechanics and optoelectronics application. They have enormous promising expectation in making flexible transistor, LED, sensor, and other optoelectronic devices which is worthy to be discovered.

1.1.4 TMDC heterostructure

Although two-dimensional single crystal TMDC materials have tremendous properties in enormous aspects, the quantum efficiency of photoelectric or electroluminescence transition are conventionally low, because of the absence of *p-n* junction in intrinsic two-dimensional single crystal TMDC material. Therefore, unequal band alignment is required for effective separation or injection of electrons and holes within a *p-n* junction.

Back in 1963, combination of two type of TMDC material, named heterostructure material, has been proposed to open up new venues in optical and optoelectronic research of semiconductor [43]. The distinction of band structure between two regions of dissimilar semiconducting material (as shown in **Figure 5**a) indicates the advantageous in engineering

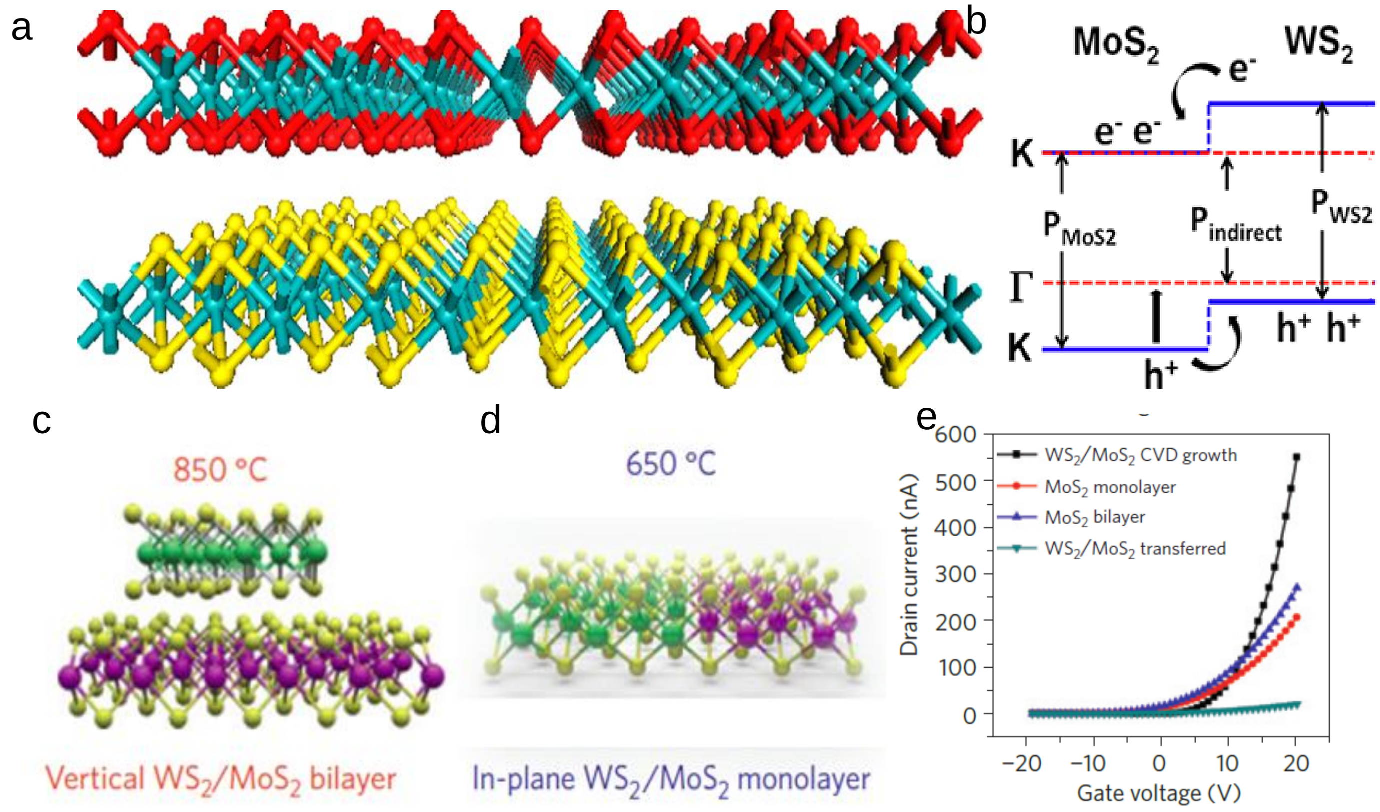

Figure 5. (a) Schematic atomic side view of typical two-dimensional multilayered heterostructure [44]. (b) The band alignment at the K-point for the WS_2/MoS_2 heterostructure. (c) Schematic images of the vertically stacked WS_2/MoS_2 heterostructures synthesized at 850℃ [45]. (d) Schematic images of the lateral connected WS_2/MoS_2 heterostructures synthesized at 650℃ [45]. (e) Typical plot of gating voltage versus source/drain current of a CVD-grown WS_2/MoS_2 bilayer, a mechanically transferred WS_2/MoS_2 bilayer, a MoS_2 bilayer and monolayer MoS_2 samples [45].

---

the electronic energy bands in many solid state device applications including semiconductor lasers, solar cells and transistors. This method was then applied on TMDC material research, in order to fulfill the further requirement and improvement of two-dimensional TMDCs. The spatial modulation and stacking of well-defined TMDC layer can achieve improvement of the chemical, optical and electronic properties of material. Moreover, unique performances such as modification of band structure (**Figure 5**b) are also demonstrated after combination of two different TMDC materials.

1.1.4.1 Type of TMDC based heterostructure

Multifarious pairs of TMDC based heterostructures have been discovered such as MoS_2/Graphene WSe_2/WS_2, $MoSe_2/MoS_2$ and WS_2/MoS_2 heterostructure. However, Among all the heterostructure, those can be generally divided into two major types, named vertical heterostructure (**Figure 5**c) and lateral heterostructure (**Figure 5**d), which demonstrate distinct properties in many aspects.

Vertical heterostructure, as illustrated in **Figure 5**c, is a common used structural arrangement that two different layers of TMDC materials are vertically overlapped with transferring method. [44-50]. Lateral heterostructure, similarly, is the combination of two different semiconductor material laterally arranged in the identical layer [45, 51-54]. The distinction between layer staking and connection would result in numerous functional differences in optical and optoelectronic devices.

Vertically heterostructure usually has large contact interface which shows large area of working region in optoelectronic devices. It can be made as atomically thin charge-separating and charge-transferring devices because of the high efficient charge transfer or separation in heterostructure, with separated electrons and holes residing in two layers upon optical excitation [48, 50]. Moreover, different stacking module of double layer heterostructure can provides different electrical and optical properties because of the correlation between physical properties of the heterostructures and orientation angle between the two layers. However, it usually has unsatisfied electrical properties as shown in **Figure 5**e, because the additional layer formed indirect bandgap is inevitable [45].

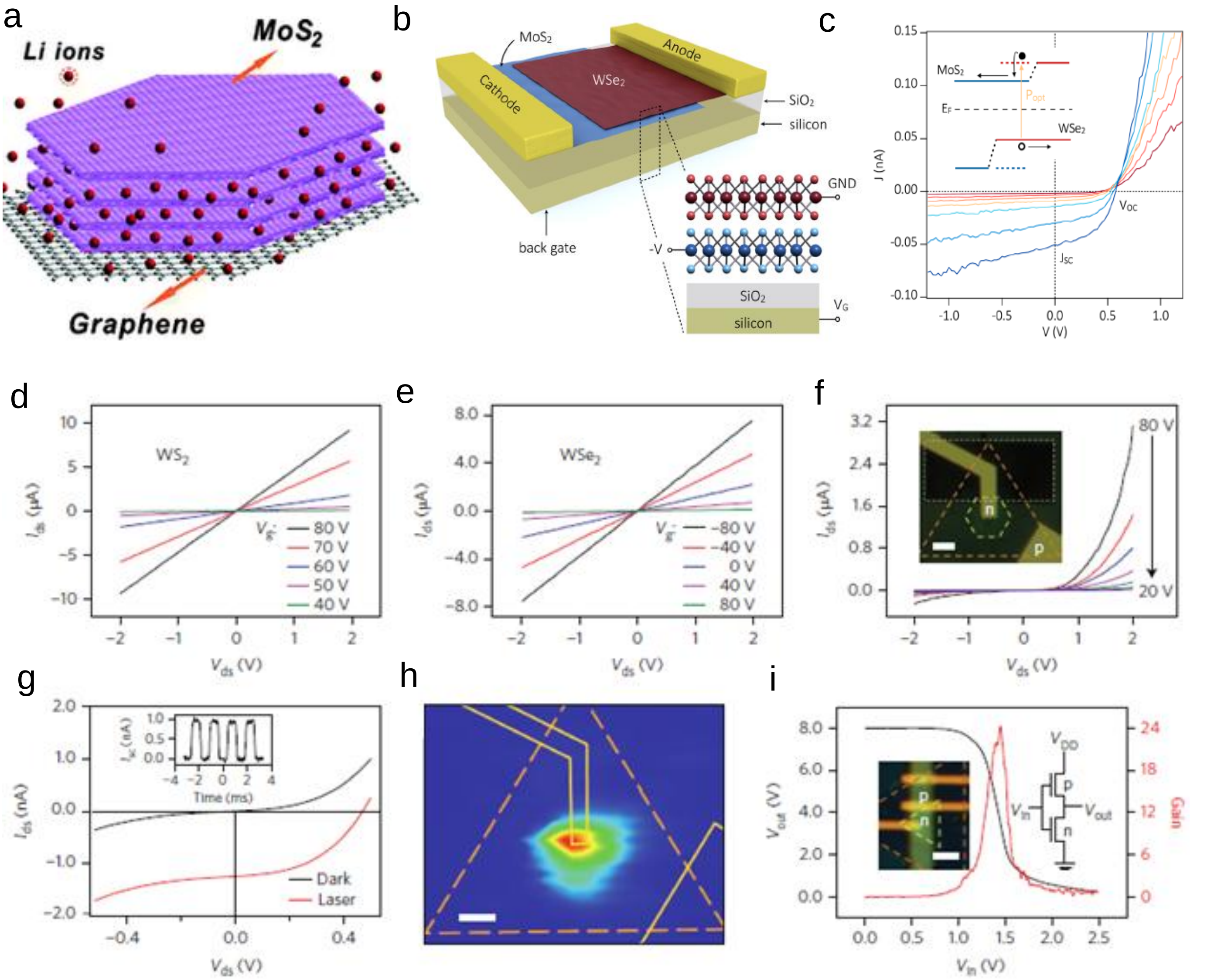

Figure 6. (a) schematic of MoS2/Graphene based Li ions battery[39]. (b) Schematic drawing of the MoS_2/WSe_2 vertical heterostructure device [49]. (c) J−V characteristics of the device under optical illumination with Popt = 180, 400, 670, 1100, 1800, 4000, and 6400 W/m2. (Inset) Schematic illustration of the photovoltaic effect [49]. (d) I_{ds}–V_{ds} output characteristics of a WS_2 FET at various backgate voltages [54]. (e), I_{ds}–V_{ds} output characteristics of a WSe_2 FET at various backgate voltages [54]. (f) Gate-tunable output characteristics of a lateral WSe_2/WS_2 heterostructure p–n diode. Scale bar, 2 µm [54]. (g) Experimental output (Ids–Vds) characteristics of the lateral WSe2–WS2 heterostructure p–n diode in the dark (black line) and under illumination (red line; wavelength, 514 nm; power, 30 nW). Inset: temporal photocurrent response under periodic on/off laser illumination through a mechanical chopper [54]. (h) Scanning photocurrent mapping image of the lateral WSe2–WS2 heterostructure p–n diode. Scale bar, 2 µm [54]. (i), A CMOS inverter obtained by integrating a p-type WSe2 and n-type WS2 FET. Scale bar, 2 µm [54].

Lateral heterostructure, on the other hand, has similar properties to that of vertical heterostructure such as *p-n* effect caused by band bending, but it is usually has high light sensitivity and better electrical properties [51, 54]. A report indicates that transistors based on lateral heterostructures exhibit much better performance than that based on vertical heterostructure, by at least three orders of magnitude in terms of intrinsic delay time and by at least two orders of magnitude in terms of transition frequency. [55]

1.1.4.2 Properties and application of TMDC heterostructure

TMDC based heterostructure have attracted substantial attention in recent years, with their outstanding, layer-number dependent photonics and electronics properties [10, 39, 44-49, 51-62]. It is not only form *p-n* junction aside the interface between two semiconductors without external bias voltage but also allows for modulation of the chemical, structural and electronic properties of two-dimensional crystals and introduces band bending for emerging in-built electric field which helps exciton dissociation.

Two-dimensional TMDC/Graphene heterostructure is one example of new system which is worthy to research (**Figure 6**a). In this system, graphene can modulate the electrical properties of TMDC and vice versa, TMDC can also modify the surface of graphene to make field effect transistor. It is reported in recent year that MoS_2/Graphene heterostructure can act as high efficient photo-catalyst for hydrogen evolution because of its high surface activity gained from the interaction between MoS_2 and graphene. Apart from that, it is also used in lithium ion battery. The coordination between MoS_2 and graphene endues the high specific capacitance of about 1100Am/g [39]

Apart from that, some efforts were made recently to create lots of types of TMDC/TMDC heterostructure, including WSe_2/WS_2 and $MoSe_2$/MoS_2, opening up exciting opportunities for the creation of a wide range of functional devices, which ranges from complementary logic circuits, photovoltaics and photodetectors, to LED and laser diodes. [49, 54]. Vertical heterostructure based on TMDC, for example, has been fabricated as a LED or FET as shown in **Figure 6**b-c. The large contact area of two TMDC materials provides large functioning region which usually increase the efficiency, providing potential for using van der Waals heterostructure in photovoltaic energy conversion. Moreover, the coupling of two layers can results in different band alignment, allowing for tuning of properties.

Lateral heterostructure on the other hand, was planning to be made as a FET, photodetector and CMOS inverter as shown **Figure 6**d-i. The monolayer of lateral arranged TMDC material usually has direct bandgap which provides better properties but few devices have been made so far, open up exciting opportunities for the creation of a wide range of functional devices, which is ranges from complementary logic circuits, photovoltaics and photodetectors, to LED and laser diodes

1.2 Preparation methods of two-dimensional material

1.2.1 Graphene preparation

Physical and chemical methods are the fundamental methods for preparation of graphene. Physical methods usually apply cheap raw material such as graphite or expanded graphite, with the micro-mechanical, liquid or gas lift-off to prepare a single layer or multi-layer graphene. This method requires raw material that is readily available and it only needs simple operation process.

1.2.1.1 Physical Method

Novoselovt et al [1] in 2004 applied a simple micro-mechanical method to successfully form graphene from peeling off of highly oriented pyrolytic graphite. The specific processes are as follows: Firstly, the oxygen plasma was applied on highly oriented pyrolytic graphite surface to etch a slot and stick it to a glass substrate. Then, they tore off the graphite with cellophane tape repeatedly. After that, the excess of highly oriented pyrolytic graphite substrate was removed and the glass with remaining single layer graphite was put into ultrasonic acetone solution. Finally, the graphene was removed with capillary force and it can be transferred on the silicon chip. However, this method has some drawbacks, such as the size of the product is not easily controlled, and it cannot reliably prepare graphene with sufficient length. Therefore, it cannot meet the needs of industrialization.

1.2.1.2 Chemical method

Chemical vapor deposition [63-68] (CVD) is a chemical reaction method with relatively high temperature. The CH_4 gas will interact with catalytic metal in the furnace to form graphene, and the resulting graphene will then deposit on the solid substrate. CVD is method that is widely used in the industry production for preparing a large-scale semiconductor thin film material. It is currently an effective way of preparing graphene with high conductivity and transparency. However, at this stage, the higher costs and complicated process of precise control of conditions hampered the development of the CVD method for graphene synthesis.

1.2.2 TMDC preparation

In order to obtain reliable production high qualified two-dimensional TMDC materials and translate them into application, numerous effective, feasible and typical production methods were applied in previous TMDC studies including top-down method like mechanical and chemical exfoliation and bottom-up method such as hydro-thermal method and CVD method.

1.2.2.1 Top -down method

Mechanical exfoliation is a top-down method which is the most traditional and simplest method to prepare two-dimensional graphene and TMDC materials. It is the representative method for separation the individual layer from bulk counterpart with strong intra-layer covalent bond and week interlayer attraction Those TMDC samples are prepared by peeling off from their parent bulk crystals with micromechanical cleavage by adhesive tape. Then, the tape with repeated-peeled material is applied to a substrate and then optically identified [13, 29, 36, 42, 69-72]. Although the morphology of resulting 2D TMDC sample of mechanical exfoliation method may not be perfectly illustrated, as shown in **Figure 2**d, the quality of it is still acceptable with few defects. The height profile of AFM result, as shown in **Figure 2**e reveals about 1nm step high which is agree with the monolayer TMDC thickness [13]. The material presents a large mobility of the order of $\mu = 10\ cm^2\ V^{-1}s^{-1}$ and a large ON/OFF ratio of the order of 10^5 according to the electrical characterisation in **figure 2**f. The major problem of this method is that it is problematic for massive production and morphology control. Low productivity of this method can only allow for modicum of samples production, for basic physical properties research.

Electric-chemical exfoliation, on the other hand, is another effective top-down method to peel bulk TMDC material into atomically thin layer with ion tension [14, 73] as shown in **Figure 2**g. During electric-chemical exfoliation, the bulk TMDC is located on the cathode and a lithium foil is attached on the anode in a battery device with water or ethanol as electrolyte. Lithium ions are inserted between TMDC layers during charging process, and release gas to separate TMDC layers during discharging process (**Figure 2**h). This method requires low temperature and procedure can be fully controlled and adjusted by referring to discharging curve. However, contamination of solution ions may be brought in and lead to changes of electric properties.

1.2.2.2 Bottom-up method

Hydro-thermal method is an outstanding bottom-up technique for synthesis of two-dimensional TMDC. It applies high temperature and pressure on the solution in an autoclave to form TMDC layered single crystal [74, 75]. WSe_2 layered TMDC material, for instance, is produced by adding Tungstic acid and selenourea into autoclave and heating in the noble gas (For example N, Ar) to 773K for 3 hours. This method can produce high quality of TMDC material with uniform size (from several nanometers to several microns) but the thickness of TMDC wafer cannot be quantitatively control so far.

CVD method is also another bottom-up method that realizes chemical reaction between vapors to form TMDC wafers at high temperature [63-68]. In order to form WS_2

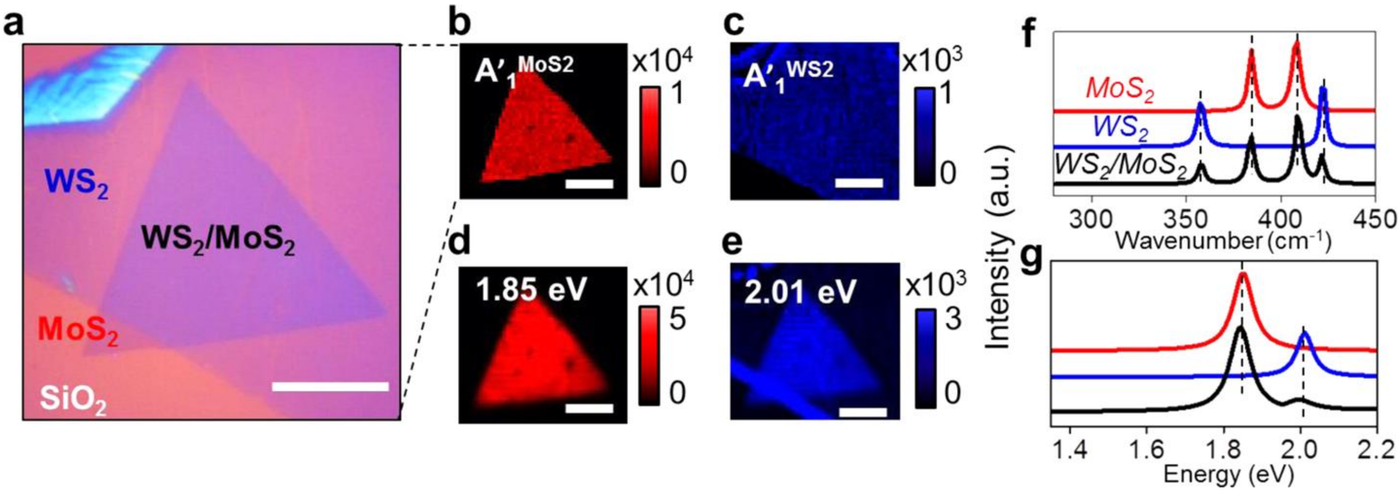

Figure 7. (a) Optical image taken from a vertical WS_2/MoS_2 heterostructure prepared by PDMS stamping of CVD grown WS_2 onto MoS_2 monolayer. (b,c) Raman mapping at the A'$_1$ mode, 408 cm^{-1} (MoS_2) and 421 cm^{-1} (WS_2), (d,e) PL mapping at 1.85 (MoS_2) and 2.01 eV (WS_2). (f) Raman and (g) PL spectra of MoS2 and WS2 monolayers and an as-transferred WS2 /MoS2 heterostructure. Scale bar is 10 μm in all figures.

---

two-dimensional material, normally, we apply precursor (S and WO3) on high temperature region and substrate (sapphire or SiO_2/Si substrate) on low temperature region in a pipe furnace. Sulphur and WO_3 is vaporized and chemical reaction happens to form WS_2. The vaporized WS2 was then deposit on substrate to form WS2 2D crystal. It is the most effective way to form large area, high quality TMDC and feasible method in thickness controlling. Therefore, it is preferred alternative for synthesis of 2D TMDC material for electronic and optical device fabrication.

This method is sensitive to the reaction parameter and condition of synthesis which need lots of research because it requires no catalyst. This method is chosen as the major methodology in synthesis of TMDC heterostructure in this report for its provided extraordinary quality of sample, which will be discussed in detailed afterwards.

1.2.3 TMDC heterostructure preparation

In order to obtain TMDC based heterostructure, production method is under investigation. Two major preparation methods, transferring method and CVD method were under discovery with efforts. Transferring method was frequently used in the early stage of the research to conventionally produce TMDC vertical heterostructure while the CVD method is frequently applied in synthesis of lateral heterostructure.

A typical transferring method for making MoS_2/WS_2 heterostructures is the PDMS stamping technique. In this process, polymers such as PDMS was spin coated on CVD grown monolayer WS_2 on substrate and dry as the transferring media. Afterwards, the coated substrate is mildly etched in KOH solution and the TMDC material is kept on polymer while gently tearing out from the substrate with help of surface tension of water. And then the PDMS/WS_2 is transferred onto targeting substrate with MoS_2. Finally, PDMS is peeled off slowly from the SiO_2/Si substrate, leaving the monolayer WS_2 on top of MoS_2. The resulting vertical heterostructure is shown in **Figure 7**a-g [46].

CVD method, however, is another typical method to directly synthesis heterostructure with high quality. According to a report, the lateral heterostructures were synthesized in home-designed CVD systems that can switch reactant during the experiment [54]. In this report, the CVD systems were designed with solid source material that can be mechanically shifted with magnet which allows for interchanging of vapor sources in and out of the hot zone. This specific design was essential to retain the active growth front for sequential hetero-epitaxial growth. The lateral heterostructure made with this method is shown in

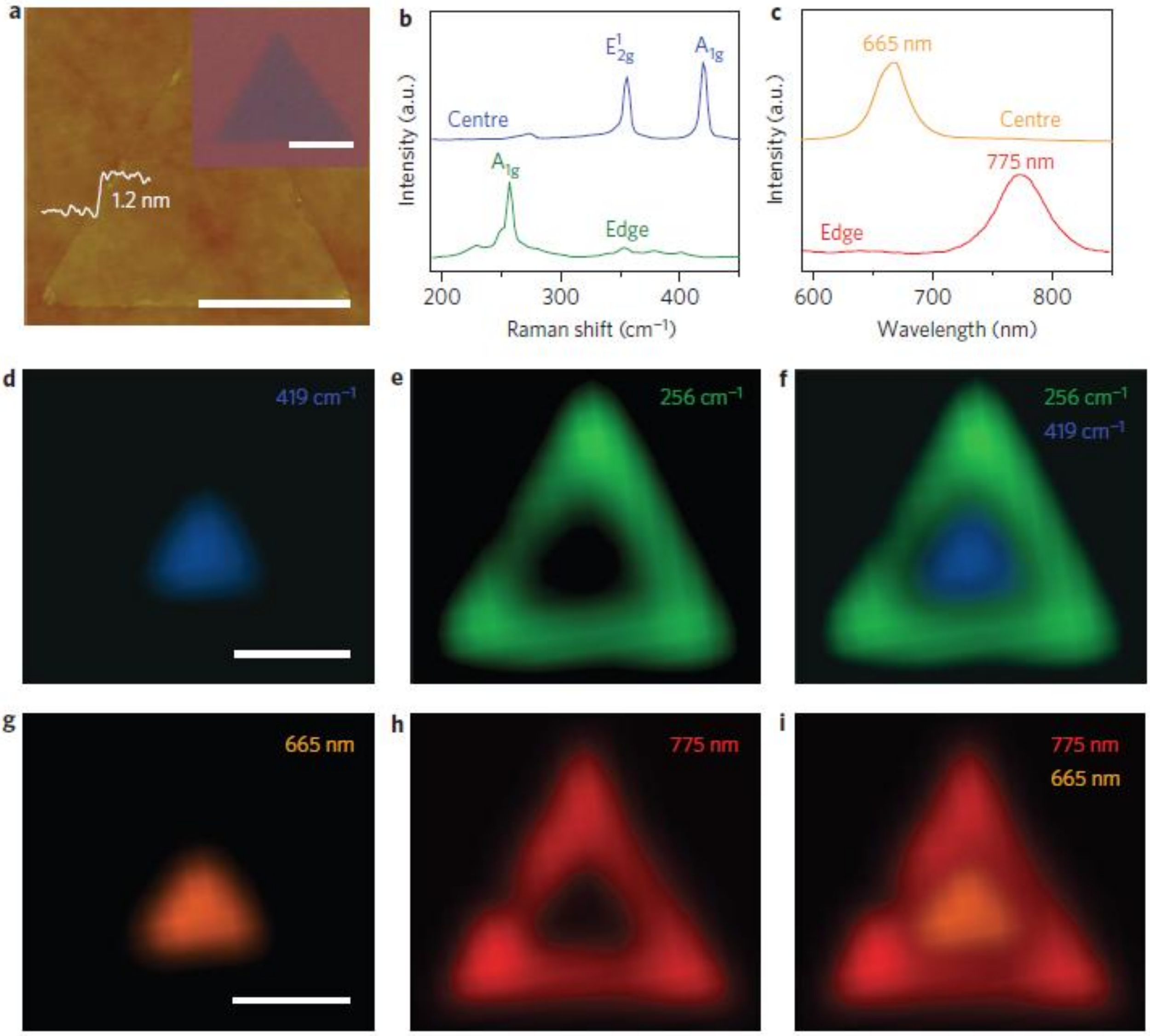

Figure 8. (a) AFM image of a triangular domain with a thickness of 1.2 nm. Inset: optical image of a triangular domain. Scale bars, 5 μm. (b) Raman spectra of a heterostructure domain. (c) Photoluminescence spectra of a heterostructure domain. (d) Raman mapping at 419 cm^{-1} (WS2 A_{1g} signal), Scale bar, 5 μm. (e) Raman mapping at 256 cm^{-1} (WSe_2 A_{1g} signal) (f), Composite image consisting of Raman mapping at 256 cm^{-1} and 419 cm^{-1}, (g-h), Photoluminescence mapping images at 665 nm and 775 nm, characteristic photoluminescence emission of WS2 and WSe2 respectively. Scale bar, 5 μm. (i) Composite image consisting of photoluminescence mapping at 665 nm and 775 nm, Scale bars in d,g apply to e,f,h,i.

Figure 8. Meanwhile, CVD "chalcogenisation" of pattern WO_3 and Mo sheets with an ambient pressure thermal reduction process is also proved to be the controllable way to produce a multilayered MoS_2/WS_2 vertical heterostructure in a large scale as shown in **Figure 9**. It applies two-step chemical vapor deposition approach to thermally deposit 5nm

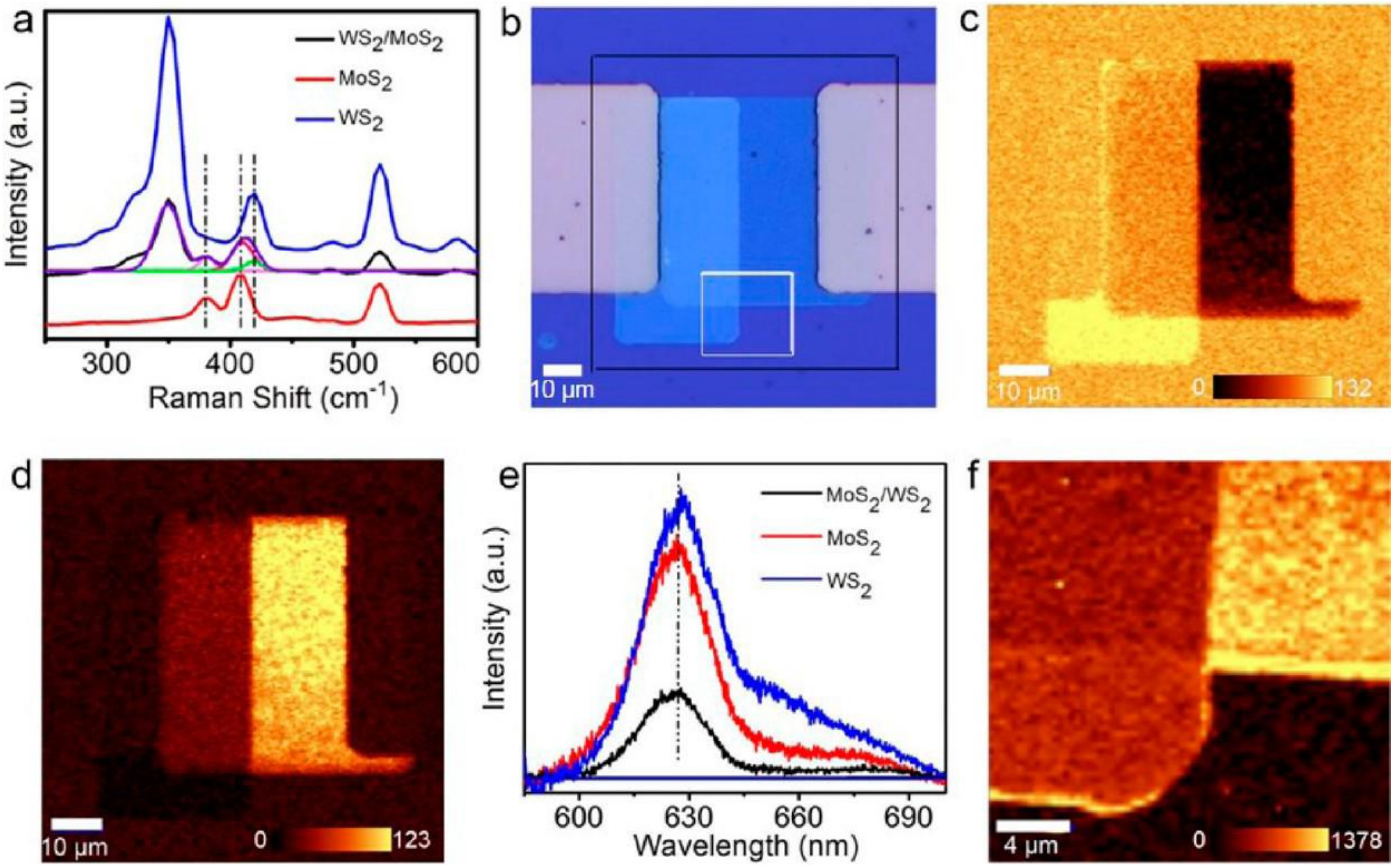

Figure 9. (a) Raman spectra of WS_2, MoS_2, and their vertical heterojunction. (b) Optical microscope images of the MoS2/WS2 vertical heterostructure device. (c,d) Raman maps of integrated intensities of peaks at 351 and 382 cm^{-1}. Data were collected from the black box in panel b, with a scanning area of 80 × 80 μm^2. (e) Single PL spectra of MoS_2, WS_2, and their vertical structure. (f) PL mapping of MoS_2/WS_2 vertical heterostructure, collected from the white box in panel b, with a scanning area of 21 × 21 $\mu m^{2.}$

---

of WO_3 and conduct sulfurisation with introducing of vaporized sulfur powder. After that, deposition of Mo layer on as-grown WS_2 layer and sulfurisation in second step is then conducted for formation of MoS_2 on the top of WS_2 [76].

In summary, the transferring method is easy and feasible way to form vertical heterostructure. Layered TMDC material growth by CVD or any other methods can be directly transferred to another TMDC with fewer defects introduced. However, contamination and residue from transferring liquid cannot be avoided. As a result, performance depreciation of transferred layer is inevitable. This method cannot make lateral heterostructure which hamper the method promotion to the public. CVD method, on the other hand, is the ideal method for synthesis of high quality TMDC lateral and vertical heterostructure. But, the non-catalyst of CVD method is sensitive to reaction parameter and condition. Precisely control of reaction condition can be problematic.

Chapter 2: Limitations, Challenges and Objective of the Thesis

2.1 Limitation of previous research

Although CVD production method of numerous types of heterostructure with various types of morphology and band structures were proposed in late 2014, and increasing number of efforts were taken in realization, characterisation and device performance researches of heterostructure, there are still problematic in TMDC heterostructure related studies.

For instance, wet transfer overlapping, one of the most typical and simplest method for synthesis of heterostructure is limited in production of vertical heterostructure and the unpredicted influences of properties are inevitably applied on transferred layer. Moreover, the indirect to direct band transition phenomenon disappears when second layer is added to another. The single-step CVD synthesis method, on the other hand, was requiring additional auxiliary equipment such as low pressure pump, movable heat region or magnet-controlled slides. Or, two-step method is required with addition heating and cooling procedure which costs unnecessary expenditure. Furthermore, extraordinary band bending was discovered in CVD formed, plane connected, monolayer heterostructure which shows disadvantage in carrier transportation and exciton disassociation.

Also, there were few optic-electronic devices fabricated and reported in the recent year, because of difficulty in micromachining on nano-scale TMDC crystal with size in a magnitude of micron. Fast oxidation, on the other hand is another major obstacle that impedes the device fabrication and characterization. Although heterostructure can brings in unique properties to TMDC material, the defects that come from process method, or galvanic effect, that from the combination of two different TMDC materials can accelerate the oxidation process.

Finally, with two different material involved in one flake, doping effect is supposed to emerge among the material, although doping effect can also endow unique properties. However, there are few people are undertaking relevant study among doping effect in the heterostructure flake. The effect of doping mode, density and cause of the doping are still undiscovered.

2.2 Challenges of the research

One of the major difficulties in two-dimensional heterostructure lies in the simply obtaining or synthesis method of high qualified corresponding TMDC heterostructure. Although the APCVD method has been applied in pure two-dimensional TMDC crystal for many years, it is still problematic for formation of designed heterostructure accurately.

On the one hand, the non-catalytic reversible reaction makes the reactants vulnerable to the high temperature environment which is necessary in CVD method. The structures of crystals are imperatively damaged by CVD heating procedure if two-step CVD method is applied, which may affect the performance of fabricated devices. On the other hand, heterostructure contains at least two types of different TMDC materials, which is unstable under high temperature, as illustrated previously. In order to protect the unstable region of firstly added

TMDC material, one-step method is supposed to applied, while it is difficult to manipulate two different constitutes properly.

Moreover, the device fabrication is another challenge of TMDC heterostructure research. Unlike the single crystalline TMDC materials, the deposited electrodes should contact with two distinct regions with different TMDC material. Precisely control of EBL for creating electrode in micron-scale requires further research among receipt of lithography and deposition of conductive metal.

2.3 Objectives of the thesis

This thesis aims at representing and showing the novel technique to produce the high qualified graded composite heterostructure via simple single-step CVD method without additional manipulation. Apart from that, it also intent to exam the as-grown constitutes-graded heterostructure via optoelectronic related test to illustrate its properties.

The unique and extraordinary properties of TMDC heterostructure have been shown previously in this report and those act as a motivation for me to grasp the knowledge of TMDC heterostructure synthesis. In order to provide large size, lateral connected and monolayered heterostructure, atmospheric-pressure chemical vapor deposition (APCVD) method was used in the thesis experiment. Meanwhile, WSe_2/WS_2 was chosen to be the first targeting heterostructure for synthesis because of the suitable band alignment. This couple of TMDC materials is less researched and possibly illustrates p-n junction with large internal electrical field which can greatly enhance the photoresponse.

The simple and feasible method is pre-requisite, since it is the premise of follow-up experiment. This method is supposed to be with simplicity of operation without any pre-designed additional devices. After the successful production of predetermined material, optimizations among experimental parameter and manipulation should be put into the consideration of experimental plan.

The characterisations of optimized heterostructure sample such as Raman, PL and AFM are then conducted to illustrate the quality and element distribution of the flake. The Raman and PL mapping should be taken to confirm the co-existence of distinct material and AFM is applied to ensure to identify the thickness. Also, the formation of two-dimensional heterostructures with graded changed composition will be investigated and a series of electronic and optoelectronic devices functional performances will be examined.

In addition, the chalcogen doping for modifying the band structure of WSe2/WS2 heterostructure is to be demonstrated with related experiment. Meanwhile, the continuous tuning of optical emission with various doping method and dopant density are supposed to be illustrated.

Chapter 3: Material synthesis procedure

Chemical vapor deposition (CVD) is a chemical synthesis method for production of high-qualified solid materials. It is widely used in semiconductor industry for producing semiconducting film [68]. A furnace is conventionally applied in CVD method for vaporizing of precursor. The volatile precursor is then push by carry gas (Argon, usually) to centre of furnace for high-temperature reaction. A targeting substrate would be exposed to vaporized reactant on the downstream of CVD system, allowing for the deposition of desired product.

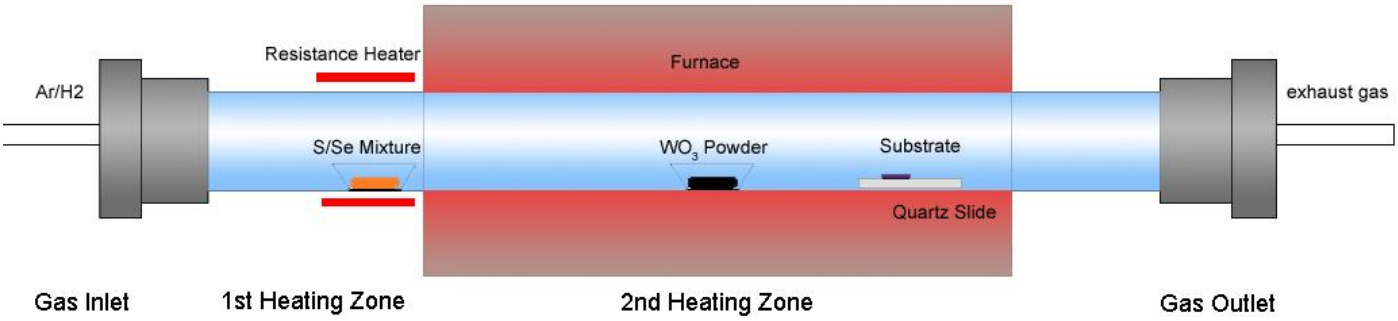

Figure 10 Schematic of CVD system

The schematic diagram of the tubing furnace CVD system for synthesis of TMDC material is shown in **Figure 10**. According to the figure, the chalcogen precursor and tungsten source are ramped to high temperature and the volatile chalcogen vapor and tungsten vapor would react to form TMDC material. The vapor of reactant is then carried by carrier gas to the downstream of furnace for solid deposition.

In this report, the growth of WSe_2/WS_2 heterostructure is performed in a typical CVD quartz tube that is isolated from outside environment. 250 sccm of argon gas at atmospheric pressure is introduced as carrier gas with another 5 sccm of hydrogen gas for reaction. the mixture of sulfur powder and Selenium powder was loaded upstream and heated independently with heating belt.WO_3 is place in the exact centre of furnace and substrate made by sapphire or SiO_2/Si (8 mm×8 mm) are placed downstream of the furnace (20 cm from the center).As shown in Figure 10, the heating belt and furnace are heated with their set profile. The heating belt is heat up to 180 ℃ for about 20 minutes and then ramped to 280 ℃ and keeps the temperature steady for more than an hour. The furnace and the sulfur are heated to 900 ℃ within 30 min are kept until the reaction stop. The furnace is then cooled naturally with the cover open.

The experiment set up for synthesis monolayer WSe_2/WS_2 heterostructure is conventionally illustrated in **Figure 12**a. The sulfur and selenium powder mixture was located in a quartz boat on upstream of the CVD system and surrounded by a heating belt in first heating region. The tungsten trioxide (WO_3) powder was loaded in the centre of tubing furnace which is marked with second heating region. The SiO_2 or sapphire substrate was put at the downstream in the second heating region and next to the Tungsten source. The heating temperature profiles of first and second heating region are indicated in **Figure 12**b. As we can see, during the growth, sulfur and selenium mixture (located in heater) was heat up to 180 ℃ for about 20 minutes and then ramped to 280 ℃ and keep the temperature steady for more than an hour. WO3 (located in furnace) was heated up to 900 ℃ and the temperature is kept until the reaction stop. The carrying gas argon was at a flow rate of 250 sccm with additional 5 sccm of H_2, and the system was operating under ambient pressure. During the reaction, the vaporized S or Se reacts with vaporized WO_3 to form WSe_2 or WS_2 and deposit on substrate downstream respectively. Because that the melting point of S and Se are different, the heating temperature change among first heating region from 180 ℃ to 280 ℃ is the core procedure that allows for different constitution distribution of S and Se in TMDC material which finally result in graded WSe_2/WS_2 heterostructure.

This graded WSe_2/WS_2 heterostructure avoid oversizing band bending which could impose disadvantage in carrier transportation, for example, the large band bending can impede the carrier transportation. Therefore, the performance of optoelectronic device, such as photodetector or LED, is worse than we expected. However, if composite is graded, t, the graded composite region acts as “ladders”, helping electrons and holes moving effectively.

For further confirmation of the morphology distinction by different growth parameter, adjusting of growth condition applied. In our experiment, we adjust the temperature holding time of CVD system from 60 mins to 120 mins for illustrate the effect of holding time.

Chapter 4: Characterisation techniques

4.1 Raman, photoluminence spectroscopy and mapping

Raman spectroscopy refers to a spectroscopic technique for observation of vibration modes with inelastic scattering, or Raman scattering, under laser light. When incident laser interacts with targeting material, the phonon scattered because of the particle vibrating. As a result, the energy of laser photons is shifted which illustrate information about the vibration modes in the system. Raman spectroscopy is commonly used in chemistry, since vibration information is specific to the chemical bonds and symmetry of molecules. Therefore, it provides a characteristic peak by which the molecule can be identified.

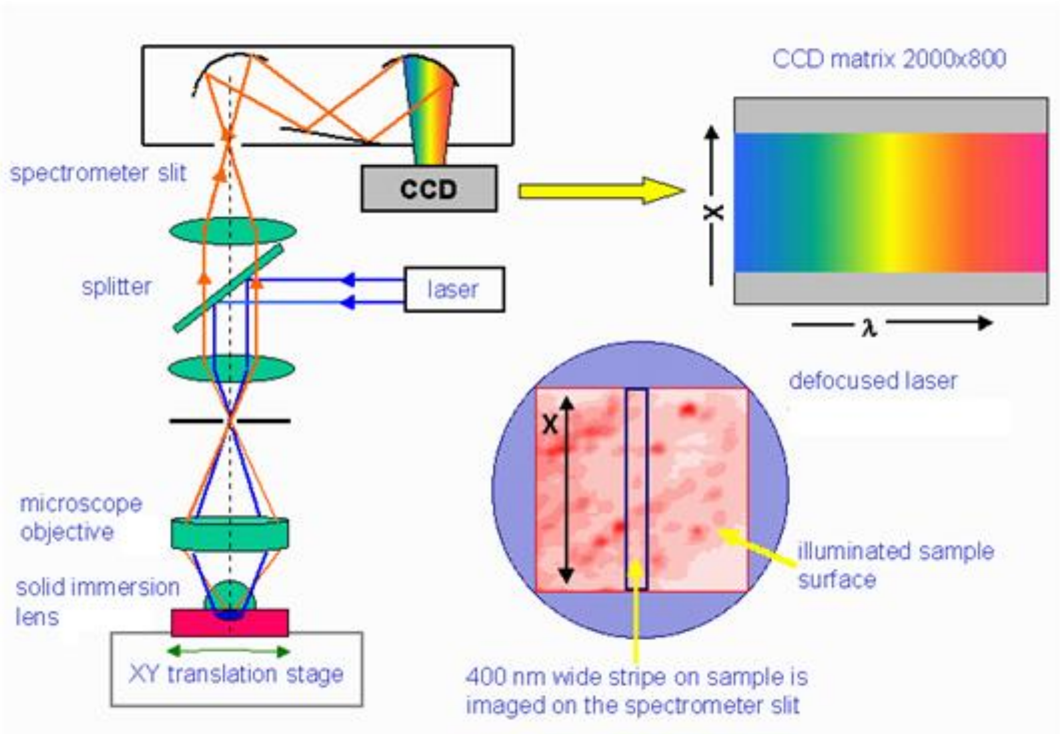

Figure 11. schematic of the PL facility [77]

Photoluminescence [77] is light emission from any form of matter after the absorption of photons. It is excited by a laser that has higher energy than the semiconductor bandgap. During excitation, the electron in valence band will jump to conduction band the drop back to valence band afterwards. Light emission happens during this excitation and drop procedure which illustrate abundant of information of semiconducting material such as bandgap, and dopant density. The facility of PL measurement can be simplified as a spectrometer and photodetector for collecting the excite electron with lenses as shown in **Figure 11**.

Raman and PL measurements were performed using confocal microscope system (WITec, alpha 300R) with a 100× objective (NA = 0.9) in an ambient condition. Laser with 532 nm wavelength was used to excite samples which were placed on a crystal-controlled scanning stage. The spectra are collected using 600 line/mm grating. To avoid the sample damage, low laser power (50 μW) is applied during the measurements.

4.2 AFM and KPFM

Atomic-force microscopy (AFM) is a system with probe scanning for illustrating information by gathering the data with a mechanical probe touching on surface. The atomic force between probe and target substrate will be amplified with torsion bar and light. Hence, it has extraordinary scanning resolution which is usually applied to precisely measurement of thickness of ultrathin layer or other recorded surface information such as phase image.

Kelvin probe force microscopy (KPFM) is a noncontact variant of AFM. KPFM using a probe tip with applied electrostatic force for probing the difference between the Fermi level and vacuum level which can reveal some internal information of band structure and electronic properties

The topography and thickness of samples were characterized by AFM (Bruker, Dimension Icon SPM) with tapping mode. The work function was measure by KPFM which is conduct on the same facility of AFM with specific tip.

4.3 XPS and SPEM

X-ray photoelectron spectroscopy (XPS) is the spectroscopic technique for measuring the elemental composition existence within a material. Beam of X-ray is applied on material to collect the electron escaping from the surface of material. SPEM, on the other hand, can be understood as the XPS mapping based on the specific XPS spectra which allows for the observation of element distribution among two-dimensional material.

For XPS and SPEM analysis, the TMDC heterostructure films are transferred to an oxide-buffered SiO2/Si wafer and kept in a ultrahigh vacuum (10^{-9} Torr), using focused soft x-rays (photon energy hν = 380 eV, beam diameter ϕ = 100 nm) generated on the beam line (SPEM end station, 09A1) of the National Synchrotron Radiation Research Center (NSRRC, Hsinchu, Taiwan)

4.4 Device fabrication and electrical measurement

The electrodes of devices were directly fabricated on heterostructure flake grown on SiO2/Si substrates. The highly doped n-type silicon of SiO2/Si substrate serves as the back gate electrode. The device fabrication includes UV lithography to define the device pattern and electron-beam evaporation to deposit source and drain electrodes (100 nm Au on top of 5 nm Ti). The measurements were performed by probe station (Cascade M150) equipped with a semiconductor property analyzer (Keithley 2400) at room temperature in ambient conditions

Chapter 5: Synthesis of WSe_2/WS_2 heterostructure and device applications

5.1 Introduction of experiment

Being considered as the potential material in next generation of electronics and optoelectornic application, ultrathin layered transition metal dichalcogenides (TMDCs) semiconductor such as Monolayer tungsten disulfide (WS_2) and tungsten diselenide (WSe_2) have attracted substantial attention in recent years, with their outstanding, layer-number dependent electronics and optoelectronic properties [11-13, 18, 20, 23-26, 28, 30, 31, 35, 64, 67, 68, 73, 78-85]. They are found to be the counterpart of graphene with reasonable high mobility and they also provide novel phenomena such as high on/off ratio, indirect to direct bandgap transition, large exciton binding energy and high photoluminescence quantum efficiency. Those properties are notably different from those of their bulk materials.

Although two-dimensional pure TMDCs have achieved much in optoelectronics and photonics, it is still challenging to release the high performance for the achievement of the industrial application. For instance, the optical properties need further tuning to fit different optoelectronic device applications, and the life time of photon-induced carrier in pure two-dimensional TMDCs are reported to be about tens of picoseconds before combination, which is relatively short compared with conventional material in III-V family [11, 20, 86]. The heterostructures based on two-dimensional TMDCs not only allows for modulation of the chemical, structural and electronic properties of two-dimensional crystals, but also introduces designed band bending for emerging in-built electric field which helps exciton separation.

In this regard, developing controllable production techniques to obtain the high quality two-dimensional TMDCs heterostructures and further optimizing the optoelectrical performance of two-dimensional TMDCs are of strategic importance, which could open new venues in optical and electronics material application as devices including light-emitting diode (LED), field effect transistor (FET) and *P-N* diodes [12, 21-30, 32, 33, 36, 37].

More recently, increasing efforts were made for realisation of numerous types of different heterostructure with various geometrical and band gap alignment. Wet Transfer overlapping technique with PMMA or PS is considered to be a simply method for creation of heterostructure with various combination but it can only provides vertical heterostructure, and lateral TMDC heterostructure synthesis is problematic and challenging in this way, on the contrary[13, 29, 36, 42, 69-72]. Two-step chemical vapor deposition (CVD) method has been successfully applied to synthesis of lateral heterostructure, but it requires additional heating and cooling procedure which is considerably costly [52, 53, 76, 87], while the single step method presented in previous work applies special designed CVD system with extra adjustment procedure [45, 51, 54]. Conventionally, this CVD made heterostructure usually has oversizing band bending which shows disadvantage in carrier transportation. Thus, a bandgap engineering of TMDC has been applied by making composition graded TMDC semiconductor to realize graded band alignment, but the method requires precursor moving during experiment, which is far more complex and hard to be manipulated [88].

In this work, we demonstrate that an ultrathin lateral WSe_2/WS_2 constitution graded heterostructure can be simply synthesized with single-step CVD growth method with plain designed equipment without any facility modifications. After that, characterisation such as optical microscopy, Raman, PL and AFM are applied to indicate the morphology, thickness and composite distribution of as-grown heterostructure. Meanwhile, electrical transport test is conduct to demonstrate some basic parameter of electronics properties such as responsivity and response rate. Compare to previous work, single step rather than two-step method is applied without pre-designed facility in our research progress, which make our operation simpler and cheaper. On the other hand, elemental substitution is introduced during the CVD growth procedure which allows for graded constitution distribution and result in the tunable bandgap gradual modification. This favors the exciton disassociation and carrier transportation, those are likely to improve the optoelectronic properties.

5.2 Characterisations

5.2.1 Optical image, Raman, PL and AFM analysis

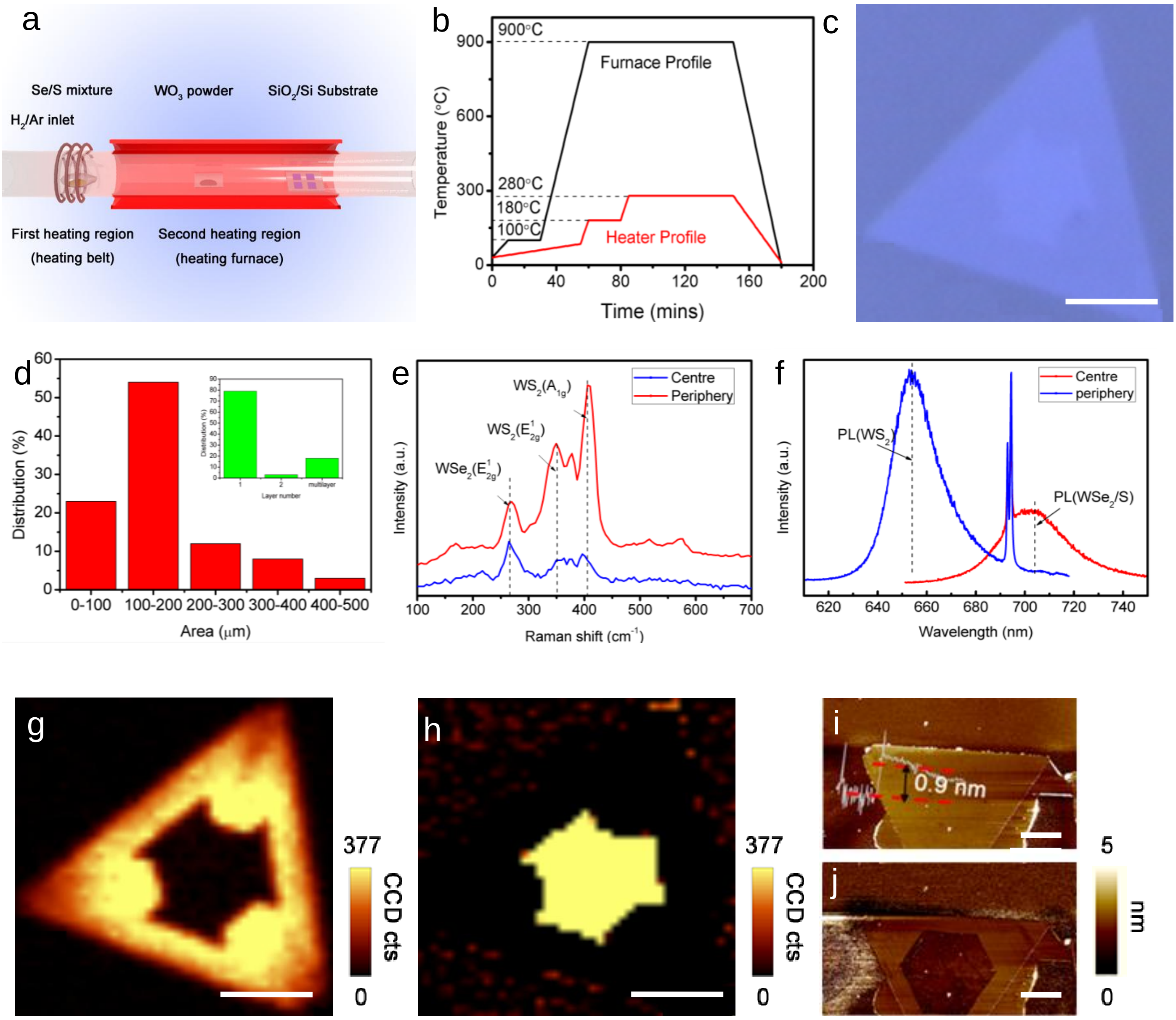

Figure 12. (a) Schematic diagram of CVD system set up for the chemical synthesis of doped WSe_2/WS_2 heterostructure. (b) Temperature profile of heating belt (first heating region) and furnace (second heating region) among growth and substitution procedure to form doped WSe_2/WS_2 heterostructure. (c) Optical Image of WSe_2/WS_2 heterostructure flake. (d) Size and thickness distribution of resulting heterostructure flake. (e) Raman spectrum which is taken from the centre and periphery region of WSe_2/WS_2 heterostructure (f) PL spectrum of doped heterostructure on the centre and edge (g-h) Raman mappings that are taken among the entire flake base on WS_2 and WSe_2 E^1_{2g} vibration mode. (The sharp peaks in the centre represent the signal of sapphire substrate) (i)AFM gained height diagram among the half of heterostructure. (the AFM sample is not the same one of Figure g and h The inset of (i) indicates the height profile along with the red dash line underneath. (j) The phase image obtained from AFM tip mode. Scale bar is 10 μm in the figure

Figure 12c shows a representative optical image of monolayer WSe_2/WS_2 lateral heterostructure on sapphire substrate synthesized by APCVD. Contrast difference between the centre and the periphery demonstrate the material differences among the entire flake. As it illustrated, the morphology of crystal is shown as hexagonal or triangular shape because of the lowest energy principle of crystal growth. They are preferentially grow along the 120° direction to locate themselves at lowest energy statue, thus a triangular or hexagonal shape is seen.

Also, the self-limited procedure of CVD reversible reaction imposes restriction on the thickness and area of TMDC flake. , the thickness and area distribution of those resulting heterostructure is illustrated in **Figure 12**d which indicates that the there are mostly single layered heterostructure flake with area of about 100-200 μm^2. To further probe the composite differences among the flake, we conduct Raman and PL studies on the WSe_2/WS_2 heterostructure.

The Raman spectra at different positions (edge and central region) are presented in **Figure 12**e. Obviously, The characteristic peak of WS_2 at 419.3 cm^{-1}, 355.4 cm^{-1}, corresponding to the $A^1{}_g$ and $E^1{}_{2g}$ resonance modes of WS_2, and characteristic peak of WSe_2 at 256.1 cm^{-1}, in agreement of the $A^1{}_g$ resonance mode of WSe_2, can be identified over the whole flake. Constitution difference can also be observed in the Raman spectra. Similarly, **Figure 12**f depicts the PL spectra of WS2-WSe2 heterostructure excited by 532 nm laser. The PL spectra for monolayer WS2 and WSe2 exhibit strong emission peak centered at ~655 nm and ~700 nm, respectively, with the outstanding PL shift in this type of heterostructure results from cations doping effect.

Those results confirm that two distinct materials, WSe_2 and WS_2, both exist in the entire flake but the composite of different regions are varied. Meanwhile, the Raman mapping studies based on the A^1_g resonance mode of WS_2 (**Fig. 12**g) and WSe_2 (**Fig. 12**h) were then conducted to further reveal the spatial distribution within the triangular domain. WSe_2 take the majority of the central region and WS_2 make up for the peripheral region of the triangular domain. AFM studies show that these two-dimensional domains typically have a thickness of ~0.9 nm (**Fig. 12**i), suggesting monolayer thickness. The phase image (**Figure 12**j) is also recorded simultaneously, which make it possible to map the refractive index for the heterostructure. The Raman mapping and AFM results imply clear interface between the two lateral contacted distinct materials without gaps or overlapping.

5.2.2 Morphology control with Raman analysis

In order to investigate the changes of morphologies and the spatial distribution of this heterostructure, we applied the Raman to mapping the sample with different growth time. **Figure 13** illustrates the morphology distinction by adjusting the temperature holding time after ramping of first region to 280 ℃. We found that the ratio of area between WSe_2 and WS_2 increases along with increasing the holding time. When holding time is about 90 mins, only a small area of WSe_2 can be found. While, when holding time increases to 120 mins, a larger area of WSe_2 triangle with only small amount of WS_2 around can be obtained. These

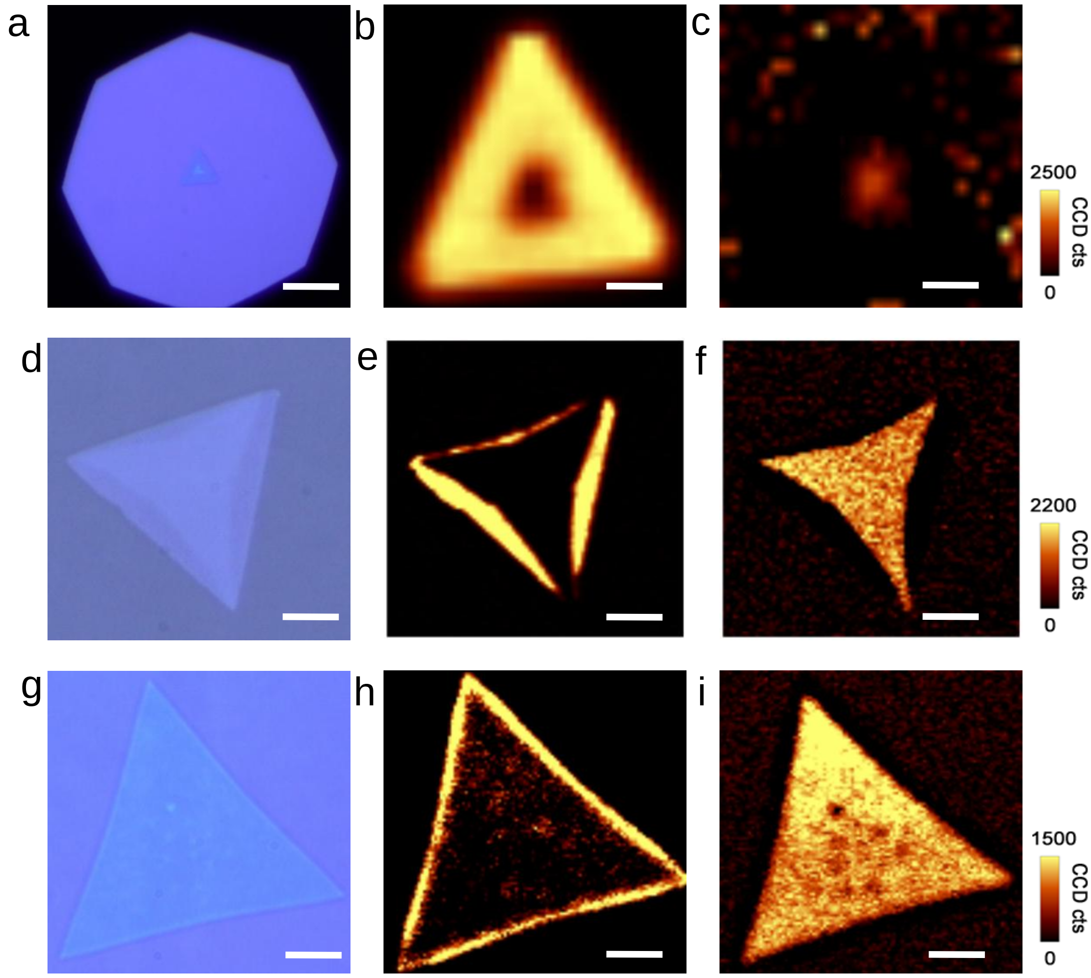

Figure 13.(a-c). The optical image of resulting heterostructure, Raman mapping of $WS_2E^1_{2g}$ vibration mode and Raman mapping of $WSe_2E^1_{2g}$ vibration mode of heterostructure that is made with holding time is about 30 minutes. (d-f) The optical image of resulting heterostructure, Raman mapping of $WS_2E^1_{2g}$ vibration mode and Raman mapping of $WSe_2E^1_{2g}$ vibration mode of heterostructure that is made with holding time is about 90 minutes. (g-i) The optical image of resulting heterostructure, Raman mapping of $WS_2E^1_{2g}$ vibration mode and Raman mapping of $WSe_2E^1_{2g}$ vibration mode of heterostructure that is made with holding time is about 90 minutes. Scale bar is 10 μm except for b and c. the scale bar of Figure b and c is 2μm.

---

indicate the possibility of morphology control with adjusting the growth time and it will reveal the knowledge of mechanism. Moreover, it provides the feasibility of spatial modulation by adjusting the area ratio with the interface change between two different TMDC materials.

5.2.3 PL shifting and KPFM analysis

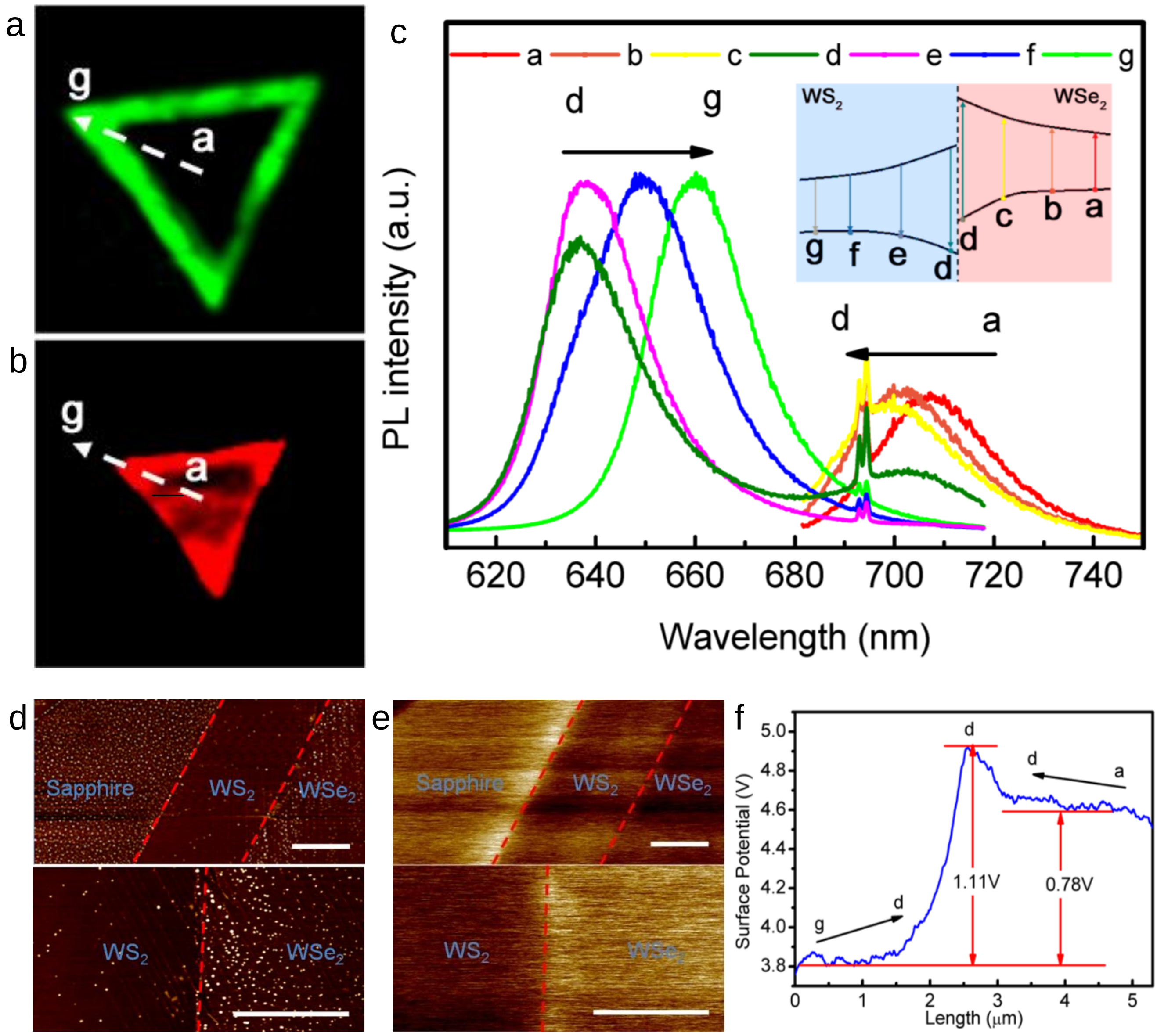

Figure 14.(a-b) PL mapping of WSe2/WS2 heterostructure based on 620nm to 680nm and based on 680nm to 740nm. Inset shows the direction of line scanning of PL spectra from a to g, the point d is located in the interface between WSe_2 and WS_2. (c) PL spectra that is taken from point a to g mark with different color. (d) AFM result among the one edge of triangular domain indicates the sapphire, WS_2 and WSe_2 (e) Surface potential mapping corresponding to AFM shown in figure 6d. (f) Surface potential profile along x-axis of figure 6e

---

In order to further demonstrate the doping effect and corresponding effect to the heterostructure, PL mapping was applied to obtain qualitative and quantitative information regarding the band structure and quantum yield efficiency for the heterostructures. The mappings of PL are taken among the spatial region 620-680 nm (doped WS2) and

680-710nm (doped WSe2) respectively (**Fig 14**a-b). Accordingly, the PL spectra are taken from different location along the dash line from centre to the edge, marked as (a) to (g), as seen from the inset of the **Figure 14**a-b. Those spectra are illustrated in **Figure 14**c and it show the position-dependent photoluminescence spectra of a single composition graded Se doped WS_2 and S doped WSe_2 in WSe_2/WS_2 heterostructure flake. From spectra a-d (d is in the interface between two domains), the spectra illustrate the continually blue-shift and from d-g, on the contrary, is red-shifted. This transverse shift can be concluded as the doping effect of Se and S which can represent the doping density. With the peak location gradually shifted when the detecting spot is moved from the center (a) to the edge (g), those position-dependent PL peak simply correspond to the change of band structure, since it is conventionally understood that the PL signal obtained from the band edge emission. This can provide the corresponding band alignment diagram (inset of **Figure 14**c), which indicates a graded band structure: The band gap increases from centre to the interface and then decreases from the interface to the edge. This observation of band shifting further prove the existence of doping elements and it further indicates that doping degree of different region are distinct since the substitution of Se start from centre and periphery in the meantime. Series of Kelvin probe force microscopy (KPFM) results (**Fig 14**d-f) indicates the surface potential change from periphery to centre. The potential is increased from edge to the interface of WSe_2/WS_2 and then decrease, which is consistent with doping constitution and bandgap change.

5.2.4 SPEM analysis

In order to further confirm the elemental arrangement of W, S and Se among the heterostructure flake, SPEM was applied to obtain the XPS mapping on W_{4f}, Se_{3d} and S_{2p} XPS spectra (**Figure 15**a-c), shown in **Figure 15**d-f. Those spectra and mapping results confirm that although the constitutional difference between WSe_2 and WS_2 can be observed in the centre and periphery, W, Se and S elements are all co-existent among the all flake. However, the multiple doping modes can be implied with those results, since the periphery contains more Se but less WSe_2 while central part is on the contrary. The interstitially doped selenium in peripheral WS_2, and substitution doping of WS_2 in central WS_2 can be further confirmed with analysis of the binding energy shift W-S and W-Se bond. The **figure 15**g-j indicates the existence of substitution doping, with the binding energy of W_{4f} and S/Se shifting to the different direction. The electronegativeity difference in S and Se element would result in the change of binding energy of W-Se and W-S bond. Hence, the energy of W and S/Se are supposed to shift to opposite direction, when the chalcogen element is replaced. However, for interstitial doping, binding energy change should be in the same direction as the nearby electronic environment has been changed by the interstitial atoms with the similar degree. As shown in **Figure 15**k-n, the binding energy shift randomly and the energy of W_{4f} and S/Se are move with the same sign. Those prove the coexistence of two

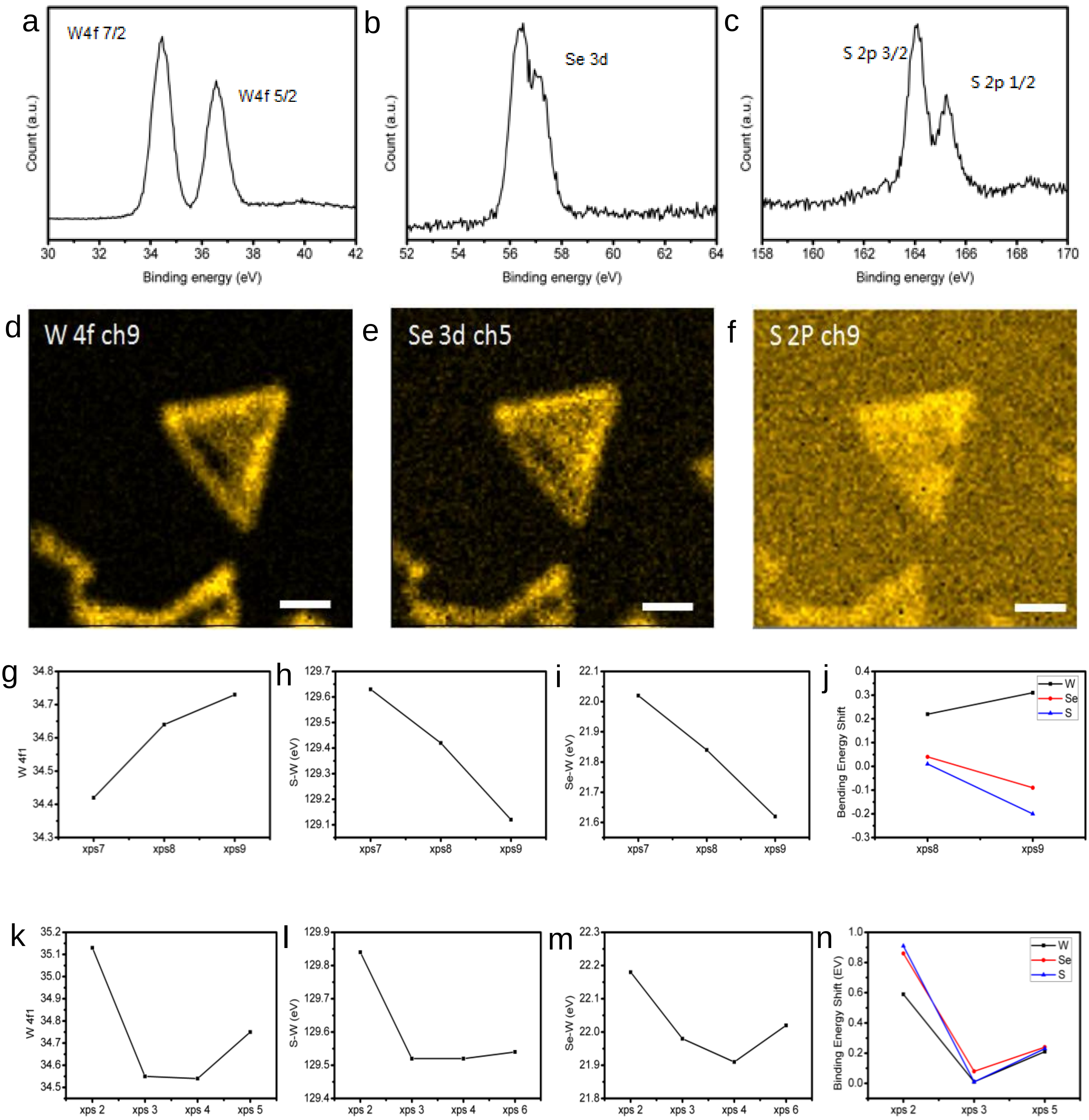

Figure 15. (a-c) XPS spectra to characteristic peak of W, Se and S (d-f) XPS mapping on W4f, Se3d and S2p element orbit with SPEM. (g-j) binding energy and binding energy shift taken from the centre of heterostructure marked with XPS 7, 8, 9. (k-n) bind energy and binding energy shift taken from the rim of heterostructure marked with XPS 2, 3, 4, 5

---

distinct doping modes, which are consistent with the previous PL and Raman results as well as the assumption of mechanism of heterostructure synthesis.

5.3 Heterostructure growth mechanism

The whole growth process can be presumably understood and followed as a procedure of growth and selectively substitution in three steps, and each stage of growth is presented in **Figure 16**a-c in corresponding experiment. Firstly, when the first heating region was about

---

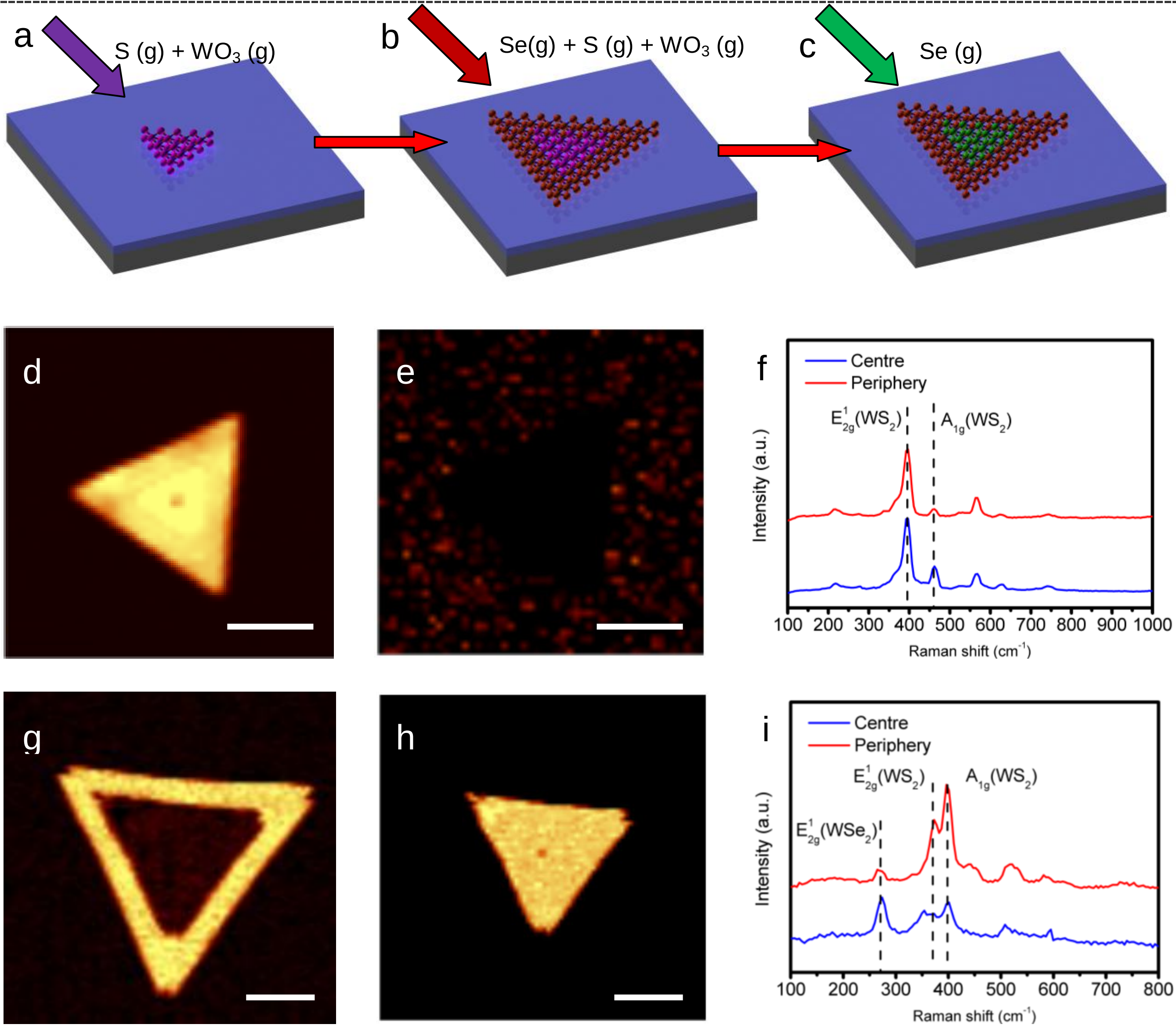

Figure 16. (a-c) Schematic diagram to show the mechanism of different growth procedure 1, 2 and 3. (d-e) Raman mapping on E^1_{2g} vibration mode of WS_2 and WSe_2 on a sample made in procedure 2. (f) Raman spectra taken from centre and periphery on a sample made in procedure 2. (g-h) Raman mapping on E^1_{2g} vibration mode of WS_2 and WSe_2 on a sample made in procedure 3. (i) Raman spectra taken from centre and periphery on a sample made in procedure 3.

180 ℃, which is lower than the melting point of Se (217 ℃), only sulfur can be vaporized from chalcogen source and flakes of pure WS_2 were only formed and grown (procedure 1). After that, when temperature of first heating zone ramp to 280 ℃, the Se source begin to melt and be vaporized. S/Se mixture steam reduces WO_3 to form WS_2 with interstitial doped Se, which was deposit on the peripheral region (procedure 2) as shown in Raman mapping of **Figure 16**d-e. The Raman spectra in **Figure 16**f indicate that there is only existence of WS_2 but the intensity distinction of E^1_{2g} between centre and periphery can be observed. In procedure 3, the S source is consumed in short time under 280 ℃ and then, only Se remains and vaporized to conduct "selenisation" of central pure WS_2 region to formed WSe_2 as illustrated in **Figure 16**g-i. This preference of reaction between Se and pure WS_2, instead of WO_3 and doped WS_2, can be owed to the chemical potential. When temperature is ignored, the Fermi level can be applied to approximately show the chemical potential for substitution reaction shown as the equation below:

$$E_{Fp} = E_v + kT\ln\frac{N_v}{N_A}$$

where the E_{Fp} stands for the chemical potential, which is usually determine the priority of reaction with different possible reactant. E_v is the energy level of valence band, k is the Boltzmann constant. T is the temperature, N_v and N_A are the effective density of states of the valence band and acceptor respectively. When Se atom is inserted into the periphery of flake to form WS_2 with Se doping, the acceptor density is increased. In this occasion, the Fermi level moves closer to the edge of the valence band, which decrease the chemical potential for reaction. Hence, the vaporized Se prefers to react with pure WS_2 in the centre instead of the periphery, and form a doped WSe_2 region in the centre.

5.4 Optoelectronic device measurements

We fabricate a field-effect transistor via electron beam lithography and focus ion beam deposition, to evaluate the electronic and photoelectric properties of this type heterostructures. **Figures 16**a illustrates the schematic diagram of fabricated device. A pair of counter electrodes is set on the heterostructure flake and each electrode is added on each domain respectively and the highly doped n-type silicon of SiO2/Si substrate serves as the back gate electrode. Typical transfer curve is shown in **Figure 16**b: With well-defined p-type characteristics in WSe_2 and n-type characteristics in WS_2, the WSe_2/WS_2 lateral heterostructure forms a natural p–n junction between the domains interface which we can see a current rectification. The optical-tunable output characteristics of a lateral WSe2/WS2 heterostructure p–n diode are shown in **Figure 16**c.

The optical power varies from 0 to 670 μW. As indicated, the current output is enhanced with increasing optical power which proves that the photocurrent is generated under light illumination and suggests that electrons prefer to migrate from WSe_2 to WS_2 to keep balance the electron potential when two types of semiconductors are lateral connected and this result in a built-in electron field at the interface. This built-in potential helps in shifting of electrons from one semiconductor to another during reduction when a positive bias is applied. On the other hand, when a negative bias is applied, the barrier is emerged and electrons cannot easily shift to inverse direction, resulting in the much smaller reverse current. It is known that this specific doped heterostructure has a graded band structure which may result in full-coverage build-in potential and helps in charge carriers transferring when positive bias is applied and act as a barrier when negative bias is applied. We also investigated the

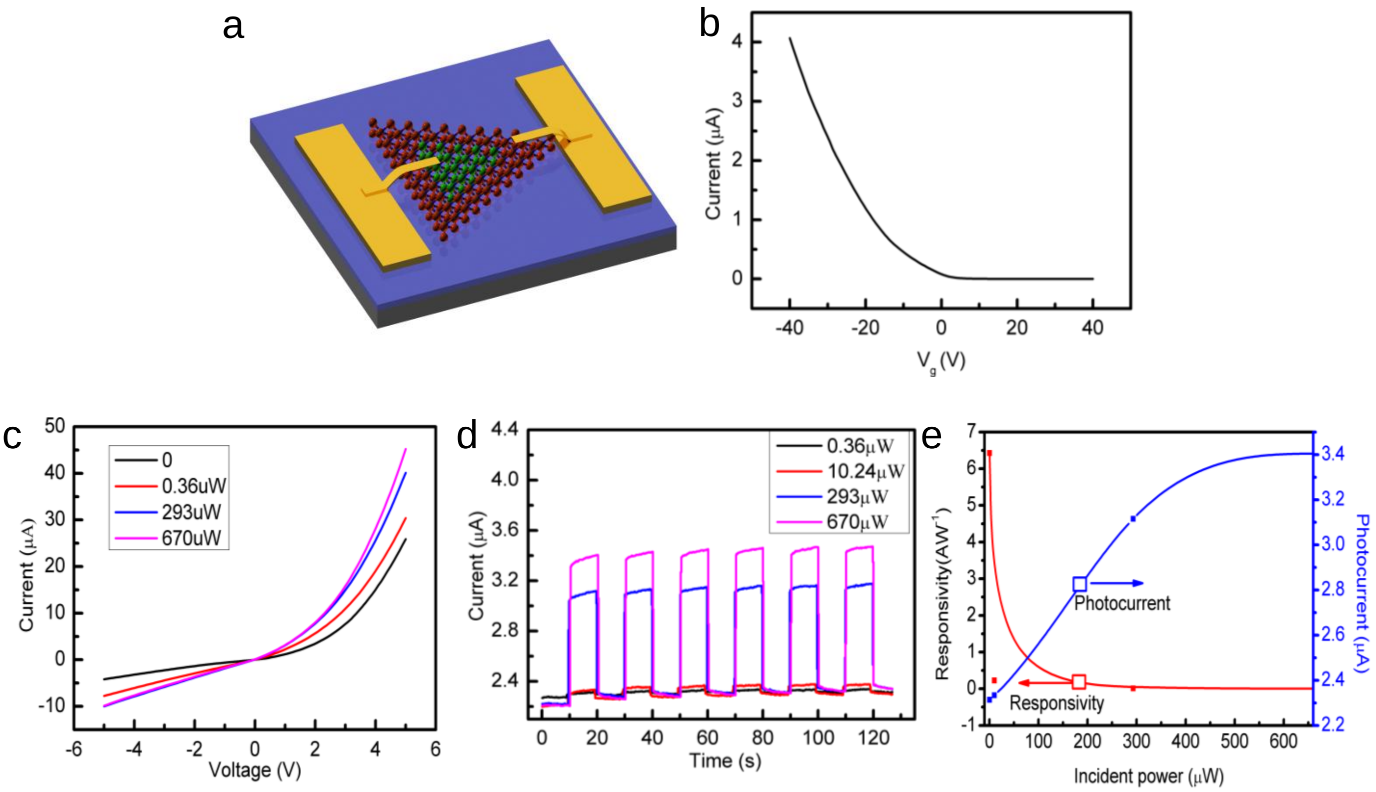

Figure 16. (a) Schematic diagram of fabricated device (b) Gate induced test. (c) Electrical transport curves (I versus V) with different light exposure, the source-drain voltage is 5V (d) Electrical photoresponse test among WSe2/WS2 heterostructure (e) Dependence of photocurrent and photoresponsivityon incident light power

---

photocurrent response to pulse light of this lateral heterostructure under various pumping power (**Fig 16**d). In general, the amplitude of photocurrent can be modulated by light power and the photoresponse exhibits a relatively rapid temporal response beyond our experimental time resolution of 300 μs, which is relatively good. The photocurrent and photo-responsivity is also illustrated in **Figure 17**e. The nonlinearly increment of photocurrent can be easily understood, whereas the photoresponsivity decreases with increasing light power with the highest photoresponsivity of 6.5 A $\cdot W^{-1}$. This may owe to the unoccupied states decrement in the conduction bands of WSe_2 and WS_2 as the power intensity increases.

Conclusion

In this report, we demonstrate a comprehensive thesis summary including literature review, research purpose, presented results, project plan and conclusion about two-dimensional TMDC heterostructure. The literature review chapter concludes the development history of two-dimensional material from finding of graphene and TMDC material to TMDC heterostructure. Those sections briefly introduce the structure, properties, preparation method and application of graphene, TMDC single crystal and TMDC heterostructure. Afterwards, research aims of project are provided as justification of necessity of relative research with my motivation, and corresponding methodology for designed research is presented. The preliminary results are then included in this report for illustration of my research progress and finding. In this section, a single step CVD growth technique is presented. It is demonstrate that ultrathin lateral WSe_2/WS_2 constitution graded heterostructure can be simply synthesized with single-step CVD growth method with plain designed equipment without any facility modification. Characterisation such as optical microscopy, Raman, PL and AFM are then applied to indicate the morphology, thickness and composite distribution of as-grown resulting heterostructure. Afterwards, morphology control with adjustment of growth parameter is presented to show the possibility of spatial

With experiment, we have successfully demonstrated the growth of ultrathin lateral contact heterostructure which is combination of doped WSe_2 and WS_2 with single step CVD chemical substitution method. Unlike other method with complex manipulation or additional procedure, this specific doped heterostructure indicates its simplified steps and easy handling access which saves time, money and provides graded constitution distribution from central part to peripheral region. Although it is not the very first discovered method, the realization of a graded composite lateral heterostructure in two-dimensional layered semiconductors can still show a new venue to apply precise constitution modulating in two-dimensional semiconductor, and it may act as a new perspective for band engineering.

Reference:

[1] K. S. Novoselov, A. K. Geim, S. V. Morozov, D. Jiang, Y. Zhang, S. V. Dubonos, *et al.*, "Electric Field Effect in Atomically Thin Carbon Films," *Science,* vol. 306, pp. 666-669, October 22, 2004 2004.

[2] A. K. Geim and K. S. Novoselov, "The rise of graphene," *Nat Mater,* vol. 6, pp. 183-191, 03//print 2007.

[3] A. A. Balandin, S. Ghosh, W. Bao, I. Calizo, D. Teweldebrhan, F. Miao, *et al.*, "Superior Thermal Conductivity of Single-Layer Graphene," *Nano Letters,* vol. 8, pp. 902-907, 2008/03/01 2008.

[4] A. B. Kuzmenko, E. van Heumen, F. Carbone, and D. van der Marel, "Universal Optical Conductance of Graphite," *Physical Review Letters,* vol. 100, p. 117401, 03/20/ 2008.

[5] G. Giovannetti, P. A. Khomyakov, G. Brocks, P. J. Kelly, and J. van den Brink, "Substrate-induced band gap in graphene on hexagonal boron nitride: \textit{Ab initio} density functional calculations," *Physical Review B,* vol. 76, p. 073103, 08/16/ 2007.

[6] Q. Bao and K. P. Loh, "Graphene Photonics, Plasmonics, and Broadband Optoelectronic Devices," *ACS Nano,* vol. 6, pp. 3677-3694, 2012/05/22 2012.

[7] J. Bai, L. Liao, H. Zhou, R. Cheng, L. Liu, Y. Huang, *et al.*, "Top-Gated Chemical Vapor Deposition Grown Graphene Transistors with Current Saturation," *Nano Letters,* vol. 11, pp. 2555-2559, 2011/06/08 2011.

[8] F. Schwierz, "Graphene transistors," *Nat Nano,* vol. 5, pp. 487-496, 07//print 2010.

[9] Y.-M. Lin, C. Dimitrakopoulos, K. A. Jenkins, D. B. Farmer, H.-Y. Chiu, A. Grill, *et al.*, "100-GHz Transistors from Wafer-Scale Epitaxial Graphene," *Science,* vol. 327, p. 662, February 5, 2010 2010.

[10] W. Fu, F.-H. Du, J. Su, X.-H. Li, X. Wei, T.-N. Ye, *et al.*, "In situ catalytic growth of large-area multilayered graphene/MoS2 heterostructures," *Sci. Rep.,* vol. 4, 04/14/online 2014.

[11] Q. H. Wang, K. Kalantar-Zadeh, A. Kis, J. N. Coleman, and M. S. Strano, "Electronics and optoelectronics of two-dimensional transition metal dichalcogenides," *Nat Nano,* vol. 7, pp. 699-712, 11//print 2012.

[12] N. Perea-López, A. L. Elías, A. Berkdemir, A. Castro-Beltran, H. R. Gutiérrez, S. Feng, *et al.*, "Photosensor Device Based on Few-Layered WS2 Films," *Advanced Functional Materials,* vol. 23, pp. 5511-5517, 2013.

[13] T. Georgiou, H. Yang, R. Jalil, J. Chapman, K. S. Novoselov, and A. Mishchenko, "Electrical and optical characterization of atomically thin WS2," *Dalton Transactions,* vol. 43, pp. 10388-10391, 2014.

[14] Z. Zeng, Z. Yin, X. Huang, H. Li, Q. He, G. Lu, *et al.*, "Single-Layer Semiconducting Nanosheets: High-Yield Preparation and Device Fabrication," *Angewandte Chemie International Edition,* vol. 50, pp. 11093-11097, 2011.

[15] D. Pacilé, J. C. Meyer, Ç. Ö. Girit, and A. Zettl, "The two-dimensional phase of boron nitride: Few-atomic-layer sheets and suspended membranes," *Applied Physics Letters,* vol. 92, p. 133107, 2008.

[16] A. D. Yoffe, "Layer Compounds," *Annual Review of Materials Science,* vol. 3, pp. 147-170, 1973.

[17] C. R. Dean, A. F. Young, MericI, LeeC, WangL, SorgenfreiS, *et al.*, "Boron nitride substrates for high-quality graphene electronics," *Nat Nano,* vol. 5, pp. 722-726, 10//print 2010.

[18] C. Ataca, H. Şahin, and S. Ciraci, "Stable, Single-Layer MX2 Transition-Metal Oxides and Dichalcogenides in a Honeycomb-Like Structure," *The Journal of Physical Chemistry C,* vol. 116, pp. 8983-8999, 2012/04/26 2012.

[19] A. Ayari, E. Cobas, O. Ogundadegbe, and M. S. Fuhrer, "Realization and electrical characterization of ultrathin crystals of layered transition-metal dichalcogenides," *Journal of Applied Physics,* vol. 101, p. 014507, 2007.

[20] S. Z. Butler, S. M. Hollen, L. Cao, Y. Cui, J. A. Gupta, H. R. Gutiérrez, *et al.*, "Progress, Challenges, and Opportunities in Two-Dimensional Materials Beyond Graphene," *ACS Nano,* vol. 7, pp. 2898-2926, 2013/04/23 2013.

[21] RadisavljevicB, RadenovicA, BrivioJ, GiacomettiV, and KisA, "Single-layer MoS2 transistors," *Nat Nano,* vol. 6, pp. 147-150, 03//print 2011.

[22] W. Zhang, M.-H. Chiu, C.-H. Chen, W. Chen, L.-J. Li, and A. T. S. Wee, "Role of Metal Contacts in High-Performance Phototransistors Based on WSe2 Monolayers," *ACS Nano,* vol. 8, pp. 8653-8661, 2014/08/26 2014.

[23] J. S. Ross, P. Klement, A. M. Jones, N. J. Ghimire, J. Yan, D. G. Mandrus, *et al.*, "Electrically tunable excitonic light-emitting diodes based on monolayer WSe2 p-n junctions," *Nat Nano,* vol. 9, pp. 268-272, 04//print 2014.

[24] S. Jo, N. Ubrig, H. Berger, A. B. Kuzmenko, and A. F. Morpurgo, "Mono- and Bilayer WS2 Light-Emitting Transistors," *Nano Letters,* vol. 14, pp. 2019-2025, 2014/04/09 2014.

[25] B. W. H. Baugher, H. O. H. Churchill, Y. Yang, and P. Jarillo-Herrero, "Optoelectronic devices based on electrically tunable p-n diodes in a monolayer dichalcogenide," *Nat Nano,* vol. 9, pp. 262-267, 04//print 2014.

[26] N. Perea-López, A. L. Elías, A. Berkdemir, A. Castro-Beltran, H. R. Gutiérrez, S. Feng, *et al.*, "Sensors: Photosensor Device Based on Few-Layered WS2 Films (Adv. Funct. Mater. 44/2013)," *Advanced Functional Materials,* vol. 23, pp. 5510-5510, 2013.

[27] O. Lopez-Sanchez, D. Lembke, M. Kayci, A. Radenovic, and A. Kis, "Ultrasensitive photodetectors based on monolayer MoS2," *Nat Nano,* vol. 8, pp. 497-501, 07//print 2013.

[28] C. Zhang, S. Wang, L. Yang, Y. Liu, T. Xu, Z. Ning, *et al.*, "High-performance photodetectors for visible and near-infrared lights based on individual WS2 nanotubes," *Applied Physics Letters,* vol. 100, p. 243101, 2012.

[29] Z. Yin, H. Li, H. Li, L. Jiang, Y. Shi, Y. Sun, *et al.*, "Single-Layer MoS2 Phototransistors," *ACS Nano,* vol. 6, pp. 74-80, 2012/01/24 2012.

[30] W. Sik Hwang, M. Remskar, R. Yan, V. Protasenko, K. Tahy, S. Doo Chae, *et al.*, "Transistors with chemically synthesized layered semiconductor WS2 exhibiting 105 room temperature modulation and ambipolar behavior," *Applied Physics Letters,* vol. 101, p. 013107, 2012.

[31] A. Kuc, N. Zibouche, and T. Heine, "Influence of quantum confinement on the electronic structure of the transition metal sulfide TS${}_{2}$," *Physical Review B,* vol. 83, p. 245213, 06/30/ 2011.

[32] K. Kaasbjerg, K. S. Thygesen, and K. W. Jacobsen, "Phonon-limited mobility in n-type single-layer MoS2 from first principles," *Physical Review B,* vol. 85, p. 115317, 03/23/ 2012.

[33] S. Kim, A. Konar, W.-S. Hwang, J. H. Lee, J. Lee, J. Yang, *et al.*, "High-mobility and low-power thin-film transistors based on multilayer MoS2 crystals," *Nat Commun,* vol. 3, p. 1011, 08/21/online 2012.

[34] Y. Ding, Y. Wang, J. Ni, L. Shi, S. Shi, and W. Tang, "First principles study of structural, vibrational and electronic properties of graphene-like MX2 (M=Mo, Nb, W, Ta; X=S, Se, Te) monolayers," *Physica B: Condensed Matter,* vol. 406, pp. 2254-2260, 5/15/ 2011.

[35] L. Leitao, S. Bala Kumar, O. Yijian, and J. Guo, "Performance Limits of Monolayer Transition Metal Dichalcogenide Transistors," *Electron Devices, IEEE Transactions on,* vol. 58, pp. 3042-3047, 2011.

[36] C. Lee, H. Yan, L. E. Brus, T. F. Heinz, J. Hone, and S. Ryu, "Anomalous Lattice Vibrations of Single- and Few-Layer MoS2," *ACS Nano,* vol. 4, pp. 2695-2700, 2010/05/25 2010.

[37] G. Eda, H. Yamaguchi, D. Voiry, T. Fujita, M. Chen, and M. Chhowalla, "Photoluminescence from Chemically Exfoliated MoS2," *Nano Letters,* vol. 11, pp. 5111-5116, 2011/12/14 2011.

[38] M. Yang, J. W. Chai, M. Callsen, J. Zhou, T. Yang, T. T. Song, *et al.*, "Interfacial Interaction between HfO2 and MoS2: From Thin Films to Monolayer," *The Journal of Physical Chemistry C,* 2016/04/20 2016.

[39] K. Chang and W. Chen, "l-Cysteine-Assisted Synthesis of Layered MoS2/Graphene Composites with Excellent Electrochemical Performances for Lithium Ion Batteries," *ACS Nano,* vol. 5, pp. 4720-4728, 2011/06/28 2011.

[40] K. F. Mak, C. Lee, J. Hone, J. Shan, and T. F. Heinz, "Atomically Thin MoS2: A New Direct-Gap Semiconductor," *Physical Review Letters,* vol. 105, p. 136805, 09/24/ 2010.

[41] Q. He, Z. Zeng, Z. Yin, H. Li, S. Wu, X. Huang, *et al.*, "Fabrication of Flexible MoS2 Thin-Film Transistor Arrays for Practical Gas-Sensing Applications," *Small,* vol. 8, pp. 2994-2999, 2012.

[42] H. Li, Z. Yin, Q. He, H. Li, X. Huang, G. Lu, *et al.*, "Fabrication of Single- and Multilayer MoS2 Film-Based Field-Effect Transistors for Sensing NO at Room Temperature," *Small,* vol. 8, pp. 63-67, 2012.

[43] H. Kroemer, "A proposed class of hetero-junction injection lasers," *Proceedings of the IEEE,* vol. 51, pp. 1782-1783,

1963.

[44] L. Kou, T. Frauenheim, and C. Chen, "Nanoscale Multilayer Transition-Metal Dichalcogenide Heterostructures: Band Gap Modulation by Interfacial Strain and Spontaneous Polarization," *The Journal of Physical Chemistry Letters,* vol. 4, pp. 1730-1736, 2013/05/16 2013.

[45] Y. Gong, J. Lin, X. Wang, G. Shi, S. Lei, Z. Lin*, et al.*, "Vertical and in-plane heterostructures from WS2/MoS2 monolayers," *Nat Mater,* vol. 13, pp. 1135-1142, 12//print 2014.

[46] S. Tongay, W. Fan, J. Kang, J. Park, U. Koldemir, J. Suh*, et al.*, "Tuning Interlayer Coupling in Large-Area Heterostructures with CVD-Grown MoS2 and WS2 Monolayers," *Nano Letters,* vol. 14, pp. 3185-3190, 2014/06/11 2014.

[47] G. W. Shim, K. Yoo, S.-B. Seo, J. Shin, D. Y. Jung, I.-S. Kang*, et al.*, "Large-Area Single-Layer MoSe2 and Its van der Waals Heterostructures," *ACS Nano,* vol. 8, pp. 6655-6662, 2014/07/22 2014.

[48] X. Hong, J. Kim, S.-F. Shi, Y. Zhang, C. Jin, Y. Sun*, et al.*, "Ultrafast charge transfer in atomically thin MoS2/WS2 heterostructures," *Nat Nano,* vol. 9, pp. 682-686, 09//print 2014.

[49] M. M. Furchi, A. Pospischil, F. Libisch, J. Burgdörfer, and T. Mueller, "Photovoltaic Effect in an Electrically Tunable van der Waals Heterojunction," *Nano Letters,* vol. 14, pp. 4785-4791, 2014/08/13 2014.

[50] F. Ceballos, M. Z. Bellus, H.-Y. Chiu, and H. Zhao, "Ultrafast Charge Separation and Indirect Exciton Formation in a MoS2–MoSe2 van der Waals Heterostructure," *ACS Nano,* vol. 8, pp. 12717-12724, 2014/12/23 2014.

[51] X.-Q. Zhang, C.-H. Lin, Y.-W. Tseng, K.-H. Huang, and Y.-H. Lee, "Synthesis of Lateral Heterostructures of Semiconducting Atomic Layers," *Nano Letters,* vol. 15, pp. 410-415, 2015/01/14 2015.

[52] Y. Yu, S. Hu, L. Su, L. Huang, Y. Liu, Z. Jin*, et al.*, "Equally Efficient Interlayer Exciton Relaxation and Improved Absorption in Epitaxial and Nonepitaxial MoS2/WS2 Heterostructures," *Nano Letters,* vol. 15, pp. 486-491, 2015/01/14 2015.

[53] C. Huang, S. Wu, A. M. Sanchez, J. J. P. Peters, R. Beanland, J. S. Ross*, et al.*, "Lateral heterojunctions within monolayer MoSe2–WSe2 semiconductors," *Nat Mater,* vol. 13, pp. 1096-1101, 12//print 2014.

[54] X. Duan, C. Wang, J. C. Shaw, R. Cheng, Y. Chen, H. Li*, et al.*, "Lateral epitaxial growth of two-dimensional layered semiconductor heterojunctions," *Nat Nano,* vol. 9, pp. 1024-1030, 12//print 2014.

[55] D. Logoteta, G. Fiori, and G. Iannaccone, "Graphene-based lateral heterostructure transistors exhibit better intrinsic performance than graphene-based vertical transistors as post-CMOS devices," *Sci. Rep.,* vol. 4, 10/20/online 2014.

[56] X. Zhang, F. Meng, J. R. Christianson, C. Arroyo-Torres, M. A. Lukowski, D. Liang*, et al.*, "Vertical Heterostructures of Layered Metal Chalcogenides by van der Waals Epitaxy," *Nano Letters,* vol. 14, pp. 3047-3054, 2014/06/11 2014.

[57] R. Cheng, D. Li, H. Zhou, C. Wang, A. Yin, S. Jiang*, et al.*, "Electroluminescence and Photocurrent Generation from Atomically Sharp WSe2/MoS2 Heterojunction p–n Diodes," *Nano Letters,* vol. 14, pp. 5590-5597, 2014/10/08 2014.

[58] K. Kośmider and J. Fernández-Rossier, "Electronic properties of the MoS2-WS2 heterojunction," *Physical Review B,* vol. 87, p. 075451, 02/28/ 2013.

[59] H.-P. Komsa and A. V. Krasheninnikov, "Electronic structures and optical properties of realistic transition metal dichalcogenide heterostructures from first principles," *Physical Review B,* vol. 88, p. 085318, 08/23/ 2013.

[60] J. Kang, J. Li, S.-S. Li, J.-B. Xia, and L.-W. Wang, "Electronic Structural Moiré Pattern Effects on MoS2/MoSe2 2D Heterostructures," *Nano Letters,* vol. 13, pp. 5485-5490, 2013/11/13 2013.

[61] T. Georgiou, R. Jalil, B. D. Belle, L. Britnell, R. V. Gorbachev, S. V. Morozov*, et al.*, "Vertical field-effect transistor based on graphene-WS2 heterostructures for flexible and transparent electronics," *Nat Nano,* vol. 8, pp. 100-103, 02//print 2013.

[62] L. Britnell, R. M. Ribeiro, A. Eckmann, R. Jalil, B. D. Belle, A. Mishchenko*, et al.*, "Strong Light-Matter Interactions in Heterostructures of Atomically Thin Films," *Science,* vol. 340, pp. 1311-1314, June 14, 2013 2013.

[63] J.-K. Huang, J. Pu, C.-L. Hsu, M.-H. Chiu, Z.-Y. Juang, Y.-H. Chang*, et al.*, "Large-Area Synthesis of Highly Crystalline

WSe2 Monolayers and Device Applications," *ACS Nano*, vol. 8, pp. 923-930, 2014/01/28 2014.

[64] C. Cong, J. Shang, X. Wu, B. Cao, N. Peimyoo, C. Qiu, *et al.*, "Synthesis and Optical Properties of Large-Area Single-Crystalline 2D Semiconductor WS2 Monolayer from Chemical Vapor Deposition," *Advanced Optical Materials,* vol. 2, pp. 131-136, 2014.

[65] Y. Zhang, Y. Zhang, Q. Ji, J. Ju, H. Yuan, J. Shi, *et al.*, "Controlled Growth of High-Quality Monolayer WS2 Layers on Sapphire and Imaging Its Grain Boundary," *ACS Nano*, vol. 7, pp. 8963-8971, 2013/10/22 2013.

[66] Y. Yu, C. Li, Y. Liu, L. Su, Y. Zhang, and L. Cao, "Controlled Scalable Synthesis of Uniform, High-Quality Monolayer and Few-layer MoS2 Films," *Sci. Rep.*, vol. 3, 05/21/online 2013.

[67] A. L. Elías, N. Perea-López, A. Castro-Beltrán, A. Berkdemir, R. Lv, S. Feng, *et al.*, "Controlled Synthesis and Transfer of Large-Area WS2 Sheets: From Single Layer to Few Layers," *ACS Nano*, vol. 7, pp. 5235-5242, 2013/06/25 2013.

[68] Y. Zhan, Z. Liu, S. Najmaei, P. M. Ajayan, and J. Lou, "Large-Area Vapor-Phase Growth and Characterization of MoS2 Atomic Layers on a SiO2 Substrate," *Small*, vol. 8, pp. 966-971, 2012.

[69] H. Li, G. Lu, Y. Wang, Z. Yin, C. Cong, Q. He, *et al.*, "Mechanical Exfoliation and Characterization of Single- and Few-Layer Nanosheets of WSe2, TaS2, and TaSe2," *Small*, vol. 9, pp. 1974-1981, 2013.

[70] J. Feng, L. Peng, C. Wu, X. Sun, S. Hu, C. Lin, *et al.*, "Giant Moisture Responsiveness of VS2 Ultrathin Nanosheets for Novel Touchless Positioning Interface," *Advanced Materials*, vol. 24, pp. 1969-1974, 2012.

[71] A. Splendiani, L. Sun, Y. Zhang, T. Li, J. Kim, C.-Y. Chim, *et al.*, "Emerging Photoluminescence in Monolayer MoS2," *Nano Letters*, vol. 10, pp. 1271-1275, 2010/04/14 2010.

[72] N. Alem, R. Erni, C. Kisielowski, M. D. Rossell, W. Gannett, and A. Zettl, "Atomically thin hexagonal boron nitride probed by ultrahigh-resolution transmission electron microscopy," *Physical Review B*, vol. 80, p. 155425, 10/12/ 2009.

[73] X. Huang, Z. Zeng, and H. Zhang, "Metal dichalcogenide nanosheets: preparation, properties and applications," *Chemical Society Reviews*, vol. 42, pp. 1934-1946, 2013.

[74] H. S. S. R. Matte, B. Plowman, R. Datta, and C. N. R. Rao, "Graphene analogues of layered metal selenides," *Dalton Transactions*, vol. 40, pp. 10322-10325, 2011.

[75] H. S. S. Ramakrishna Matte, A. Gomathi, A. K. Manna, D. J. Late, R. Datta, S. K. Pati, *et al.*, "MoS2 and WS2 Analogues of Graphene," *Angewandte Chemie International Edition*, vol. 49, pp. 4059-4062, 2010.

[76] Y. Xue, Y. Zhang, Y. Liu, H. Liu, J. Song, J. Sophia, *et al.*, "Scalable Production of a Few-Layer MoS2/WS2 Vertical Heterojunction Array and Its Application for Photodetectors," *ACS Nano*, vol. 10, pp. 573-580, 2016/01/26 2016.

[77] S. M. K.P. Hewaparakrama, H.E. Jackson, L.M. Smith, G. Karczewski, J. Kossut, "Photoluminescence Imaging of CdTe/ZnTe Self-Assembled Quantum Dots," in *AIP Conference Proceedings*, 2005.

[78] G. Wang, X. Marie, L. Bouet, M. Vidal, A. Balocchi, T. Amand, *et al.*, "Exciton dynamics in WSe2 bilayers," *Applied Physics Letters*, vol. 105, p. 182105, 2014.

[79] A. Chernikov, T. C. Berkelbach, H. M. Hill, A. Rigosi, Y. Li, O. B. Aslan, *et al.*, "Exciton Binding Energy and Nonhydrogenic Rydberg Series in Monolayer WS2," *Physical Review Letters*, vol. 113, p. 076802, 08/13/ 2014.

[80] W. Zhao, R. M. Ribeiro, M. Toh, A. Carvalho, C. Kloc, A. H. Castro Neto, *et al.*, "Origin of Indirect Optical Transitions in Few-Layer MoS2, WS2, and WSe2," *Nano Letters*, vol. 13, pp. 5627-5634, 2013/11/13 2013.

[81] P. Tonndorf, R. Schmidt, P. Böttger, X. Zhang, J. Börner, A. Liebig, *et al.*, "Photoluminescence emission and Raman response of monolayer MoS2, MoSe2, and WSe2," *Optics Express*, vol. 21, pp. 4908-4916, 2013/02/25 2013.

[82] J.-G. Song, J. Park, W. Lee, T. Choi, H. Jung, C. W. Lee, *et al.*, "Layer-Controlled, Wafer-Scale, and Conformal Synthesis of Tungsten Disulfide Nanosheets Using Atomic Layer Deposition," *ACS Nano*, vol. 7, pp. 11333-11340, 2013/12/23 2013.

[83] A. M. Jones, H. Yu, N. J. Ghimire, S. Wu, G. Aivazian, J. S. Ross, *et al.*, "Optical generation of excitonic valley coherence in monolayer WSe2," *Nat Nano*, vol. 8, pp. 634-638, 09//print 2013.

[84] H. R. Gutiérrez, N. Perea-López, A. L. Elías, A. Berkdemir, B. Wang, R. Lv, *et al.*, "Extraordinary Room-Temperature

Photoluminescence in Triangular WS2 Monolayers," *Nano Letters*, vol. 13, pp. 3447-3454, 2013/08/14 2013.

[85] D. Tonti, F. Varsano, F. Decker, C. Ballif, M. Regula, and M. Remškar, "Preparation and Photoelectrochemistry of Semiconducting WS2 Thin Films," *The Journal of Physical Chemistry B*, vol. 101, pp. 2485-2490, 1997/04/01 1997.

[86] H. Wang, C. Zhang, and F. Rana, "Surface Recombination Limited Lifetimes of Photoexcited Carriers in Few-Layer Transition Metal Dichalcogenide MoS2," *Nano Letters*, vol. 15, pp. 8204-8210, 2015/12/09 2015.

[87] M.-Y. Li, Y. Shi, C.-C. Cheng, L.-S. Lu, Y.-C. Lin, H.-L. Tang, *et al.*, "Epitaxial growth of a monolayer WSe2-MoS2 lateral p-n junction with an atomically sharp interface," *Science*, vol. 349, pp. 524-528, 2015-07-31 00:00:00 2015.

[88] H. Li, Q. Zhang, X. Duan, X. Wu, X. Fan, X. Zhu, *et al.*, "Lateral Growth of Composition Graded Atomic Layer MoS2(1–x)Se2x Nanosheets," *Journal of the American Chemical Society*, vol. 137, pp. 5284-5287, 2015/04/29 2015.